Unveiling the formation of the massive DR21 ridge

Bonne, L.; Bontemps, S.; Schneider, N.; Simon, R.; Clarke, S.D.; Csengeri, T.; ... ; Tiwari, M.

Citation

Bonne, L., Bontemps, S., Schneider, N., Simon, R., Clarke, S. D., Csengeri, T., ... Tiwari, M. (2023). Unveiling the formation of the massive DR21 ridge. *The Astrophysical Journal*, *951*(1). doi:10.3847/1538-4357/acd536

The Astrophysical Journal, 951:39 (26pp), 2023 July 1 https://doi.org/10.3847/1538-4357/acd536

Unveiling the Formation of the Massive DR21 Ridge

L. Bonne[1], S. Bontemps[2], N. Schneider[3], R. Simon[3], S. D. Clarke[4], T. Csengeri[2], E. Chambers[1], U. Graf[3],
J. M. Jackson[1,5], R. Klein[1], Y. Okada[3], A. G. G. M. Tielens[6,7], and M. Tiwari[6]
[1] SOFIA Science Center, NASA Ames Research Center, Moffett Field, CA 94045, USA; lbonne@usra.edu
[2] Laboratoire d'Astrophysique de Bordeaux, Université de Bordeaux, CNRS, B18N, allée Geoffroy Saint-Hilaire, F-33615 Pessac, France
[3] I. Physikalisches Institut, Universität zu Köln, Zülpicher Str. 77, D-50937 Köln, Germany
[4] Academia Sinica, Institute of Astronomy and Astrophysics, Taipei, Taiwan
[5] Green Bank Observatory, P.O. Box 2, Green Bank, WV 24944, USA
[6] University of Maryland, Department of Astronomy, College Park, MD 20742-2421, USA
[7] Leiden Observatory, P.O. Box 9513, 2300 RA Leiden, The Netherlands

Received 2022 October 28; revised 2023 May 2; accepted 2023 May 12; published 2023 July 10

Abstract

We present new ^{13}CO (1–0), C^{18}O (1–0), HCO$^+$ (1–0), and H^{13}CO$^+$ (1–0) maps from the IRAM 30 m telescope and a spectrally resolved [C II] 158 μm map observed with the SOFIA telescope toward the massive DR21 cloud. This traces the kinematics from low- to high-density gas in the cloud, which allows us to constrain the formation scenario of the high-mass star-forming DR21 ridge. The molecular line data reveal that the subfilaments are systematically redshifted relative to the dense ridge. We demonstrate that [C II] unveils the surrounding CO-poor gas of the dense filaments in the DR21 cloud. We also show that this surrounding gas is organized in a flattened cloud with curved redshifted dynamics perpendicular to the ridge. The subfilaments thus form in this curved and flattened mass reservoir. A virial analysis of the different lines indicates that self-gravity should drive the evolution of the ridge and surrounding cloud. Combining all results, we propose that bending of the magnetic field, due to the interaction with a mostly atomic colliding cloud, explains the velocity field and resulting mass accretion on the ridge. This is remarkably similar to what was found for at least two nearby low-mass filaments. We tentatively propose that this scenario might be a widespread mechanism to initiate star formation in the Milky Way. However, in contrast to low-mass clouds, gravitational collapse plays a role on the parsec scale of the DR21 ridge because of the higher density. This allows more effective mass collection at the centers of collapse and should facilitate massive cluster formation.

Unified Astronomy Thesaurus concepts: Molecular clouds (1072); Interstellar medium (847); Star formation (1569)

1. Introduction

The formation of massive stars is still a matter of intense debate (e.g., Zinnecker & Yorke 2007; Tan et al. 2014; Motte et al. 2018a). The very short, or potentially nonexisting, massive prestellar core phase (e.g., Motte et al. 2007, 2010; Russeil et al. 2010; Csengeri et al. 2014; Tigé et al. 2017; Sanhueza et al. 2019) suggests that high-mass stars might not form from the quasi-static evolution toward collapse of individual prestellar cores. This opens the question of how massive stars can form. Based on observations of molecular clouds that form massive stars, it was proposed that some large-scale dynamics, partly driven by self-gravity, can provide the fast concentration of mass necessary to form massive stars (e.g., Peretto et al. 2006, 2013, 2014; Hartmann & Burkert 2007; Galván-Madrid et al. 2010; Schneider et al. 2010, 2015; Csengeri et al. 2011a, 2011b; Wyrowski et al. 2012, 2016; Beuther et al. 2015; Williams et al. 2018; Jackson et al. 2019; Bonne et al. 2022a).

This probable coupling to the molecular cloud dynamics is also put forward by several theoretical models. In the competitive accretion model (Bonnell et al. 2001, 2004; Bonnell & Bate 2006; Wang et al. 2010), the gravitational pull of low-mass protostellar cores drives the mass accretion from the surrounding cloud to determine their final mass. The fragmentation-induced starvation scenario proposes that massive stars form through gravitational fragmentation at the center of dense filamentary accretion flows (Peters et al. 2010, 2011; Girichidis et al. 2012), where the fragmentation in the inflowing filaments sets a limit on the accretion of the most massive stars at the center of the accretion flow. Another variant proposes that gravitational collapse on multiple scales after the thermal instability (Vázquez-Semadeni et al. 2009, 2017, 2019) drives the required dynamics and mass concentration responsible for the formation of massive stars, which is then halted by stellar feedback. From simulations it was also proposed that compression by the collision of atomic flows or fully developed molecular clouds at high velocities can form dense filamentary structures that host massive star formation (e.g., Dobbs et al. 2012, 2020; Inoue & Fukui 2013; Wu et al. 2015; Balfour et al. 2017; Bisbas et al. 2017). The velocity and density of the H I flows or molecular clouds would then be decisive to determine whether massive stars can form. Typically, collision velocities >10 km s^{-1} would be needed to form massive stars (Haworth et al. 2015; Dobbs et al. 2020). Based on observed bridging with CO lines between separated velocity components in several clouds, it has been proposed that cloud–cloud collisions (CCCs) might play a role in high-mass star formation (e.g., Bisbas et al. 2018; Fukui et al. 2021; Lim et al. 2021). From simulations, it was also proposed that an oblique shock associated with collision velocities above 7 km s^{-1} could bend the magnetic field around the filaments and drive subsequent mass inflow that enables high-mass star formation (Inoue et al. 2018; Abe & Inoue 2021).

Analyzing observations of the low-mass Musca filament and the surrounding Chamaeleon−Musca regions, Bonne et al. (2020a, 2020b) concluded that continuous mass accretion on the Musca filament was driven by such bending of the magnetic field owing to a 50 pc scale collision at ∼7 km s^{-1} between H I clouds in the Chamaeleon−Musca complex. This mechanism was proposed for the formation of high-mass star-forming filaments (Inoue et al. 2018) but might also be applicable for low-mass star-forming filaments. Specifically, the Musca filament would be the result of a turbulent overdensity that is compressed and guided by the bended magnetic field during interaction with more diffuse gas in the colliding cloud. Interestingly, Faraday rotation measurements in the radio domain, which trace the magnetic field properties in the interstellar medium (ISM), unveiled curved magnetic fields around several nearby low-to-intermediate-mass star-forming regions (Tahani et al. 2019, 2022). It also unveiled a correlation of the cold neutral medium and lukewarm neutral medium with the magnetic field structure in the diffuse ISM (Bracco et al. 2020). These results would have a straightforward explanation in the proposed scenario of colliding H I clouds that bend the magnetic field. Furthermore, recent observations of the massive star-forming cloud NGC 6334 found kinematic structure resembling the results in Musca (Arzoumanian et al. 2022).

In this paper, we present a multiwavelength study of the DR21 cloud in molecular and atomic lines and dust continuum to follow up on the link between molecular cloud evolution and the formation of dense filamentary structures. Specifically, after focusing on Musca, we now focus on a region where massive stars are currently forming. The DR21 cloud is located in the north of the Cygnus X molecular cloud complex (Reipurth & Schneider 2008) at an estimated distance of ∼1.4 kpc (Rygl et al. 2012). This cloud hosts the DR21 ridge, which is the filamentary structure with a length of ∼4 pc and a mass of $\sim 10^4\ M_\odot$ that is typically defined by high column densities, i.e., $N_{H_2} > 10^{23}$ cm^{-2} (Schneider et al. 2010; Hennemann et al. 2012). The DR21 ridge is the densest and most massive filament in the entire Cygnus X complex and one of the most active high-mass star-forming regions within 2 kpc from the Sun (Kumar et al. 2007; Motte et al. 2007; Beerer et al. 2010; Bontemps et al. 2010; Csengeri et al. 2011a, 2011b; Duarte-Cabral et al. 2013, 2014). In this paper, we will use the term "ridge" for the inner, high column density part ($N_{H_2} > 10^{23}$ cm^{-2}) of the molecular cloud (Hill et al. 2011, 2012), "subfilaments" for the lower-density filaments connected to the ridge, and "cloud" for the parsec-scale surrounding cloud that includes the ridge.

Detailed kinematic studies of the DR21 region by Schneider et al. (2010) demonstrated that the ridge is experiencing large-scale gravitational collapse and mass accretion by subfilaments that run parallel to the magnetic field (Vallée & Fiege 2006; Ching et al. 2022). Figure 1 shows the DR21 cloud and ridge ($N_{H_2} > 10^{23}$ cm^{-2}) and the subfilaments defined in Schneider et al. (2010) and Hennemann et al. (2012). It is also proposed that the DR21 cloud is part of the Cygnus X complex, which forms a single region with multiple velocity components (Schneider et al. 2006, 2007). This was later confirmed by Rygl et al. (2012) and provided arguments that DR21 is the result of a collision between two molecular clouds with velocity components at ∼−3 and 9 km s^{-1} (Dickel et al. 1978; Dobashi et al. 2019). This collision is revisited and discussed in Schneider et al. (2023) using new insight from the SOFIA [C II] data.

In this paper, we aim to establish the main processes, i.e., gravity, magnetic field, and turbulence, that drive the evolution of this massive star-forming molecular cloud from low-density ($n_{H_2} \lesssim 10^3$ cm^{-3}) gas in the surrounding cloud to high-density ($n_{H_2} > 10^5$ cm^{-3}) gas in the ridge. In Section 2, we give observational details. Section 3 presents the observational results of the DR21 cloud, followed by the inflow and virial analysis of these observational results in Section 4. Lastly, in Section 5 we put these results into context to propose a scenario for the DR21 cloud evolution and discuss how it compares to low-mass star-forming clouds.

2. Observations

The observations tracing different density regimes in the DR21 cloud are described in the following subsections and are summarized in Table 1.

2.1. IRAM 30 m Observations

Observations with the IRAM 30 m telescope of the DR21 region (surrounding cloud, ridge and subfilaments) were carried out in 2015 February. These observations were performed with two different spectral setups using the FTS50 configuration of the EMIR receiver. Setup 1, which contains HCO^+ (1−0) and $H^{13}CO^+$ (1−0), covers the spectral ranges ∼85.2–87.2 GHz, 88.5–90.5 GHz, 101.0–102.8 GHz, and 104.2–106.0 GHz. Setup 2, which contains ^{13}CO (1−0) and $C^{18}O$ (1−0), covers the spectral ranges ∼89.6–91.6 GHz, 93.0–95.0 GHz, 105.4–107.2 GHz, and 108.8–110.6 GHz. These two setups allow us to observe a variety of molecular lines (e.g., $C^{18}O$ (1−0), N_2H^+ (1–0), HCN (1–0), HCO^+ (1−0), NH_2D [1(1,1)0−1(0,1)0], etc.), which allows us to follow the kinematic and chemical evolution of the dense gas in the DR21 ridge and the connected subfilaments. The obtained antenna temperature (T_A^*) noise rms within a spectral resolution of 0.2 km s^{-1} is ∼0.14 K around 90 GHz and ∼0.20 K around 110 GHz, respectively. A main-beam efficiency of 0.81 for frequencies around 90 GHz and 0.78 for frequencies around 110 GHz was used (Kramer et al. 2013). The region on the sky that is covered by the two different setups is displayed in Figure 1. The mapping was performed in the on-the-fly (OTF) observing mode, and the resulting data cubes have a spatial resolution between ∼23″ (110 GHz) and ∼29″ (90 GHz); see Table 1. To produce the data cubes, a first-order baseline was fitted to the data with CLASS in GILDAS,[8] as the baselines are generally well behaved at the observed frequencies. A full analysis of all the lines that are covered will be the topic of a future paper. Here the first results from ^{13}CO (1−0), $C^{18}O$ (1−0), HCO^+ (1−0), and $H^{13}CO^+$ (1−0) will be presented.

2.2. SOFIA [C II] Observations with UpGREAT

To obtain a more complete view on the kinematics of the DR21 cloud, the IRAM observations are combined with observations of the [C II] 158 μm line by the Stratospheric Observatory for Infrared Astronomy (SOFIA; Young et al. 2012). The [C II] observations at 158 μm were taken as part of the SOFIA Legacy program FEEDBACK,[9] which maps 11

---

[8] https://www.iram.fr/IRAMFR/GILDAS/

[9] https://feedback.astro.umd.edu

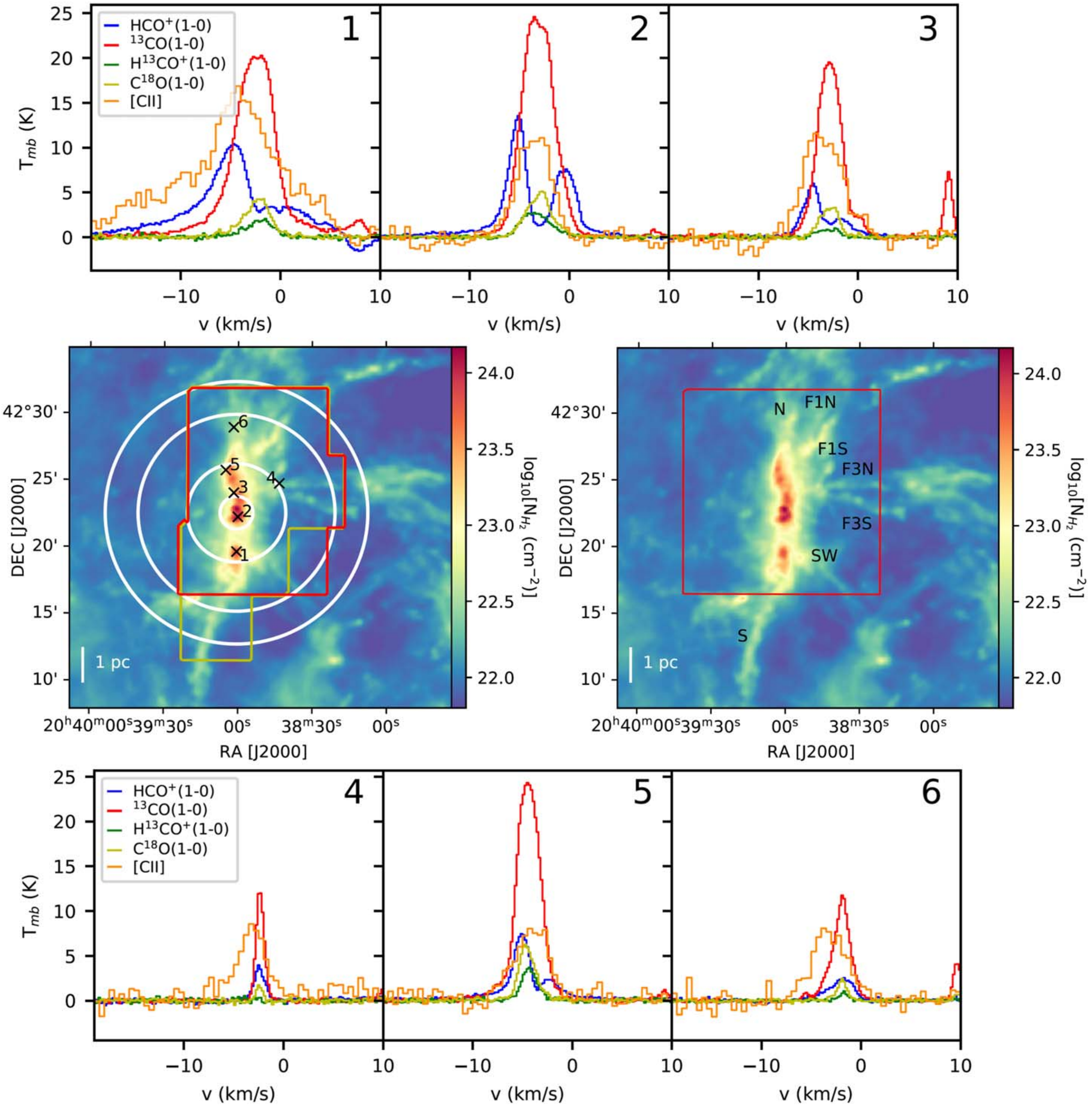

Figure 1. Middle left: Herschel column density map (Hennemann et al. 2012) of the DR21 cloud (ridge and surrounding subfilaments). The yellow and red polygons indicate the area covered by the two different backend setups of the IRAM 30 m observations, i.e., setup 1 (yellow) and setup 2 (red). The southern subfilament is only covered by the first setup, which contains HCO^+ (1−0) and $H^{13}CO^+$ (1−0). The crosses indicate the location of the spectra displayed in the bottom and top panels. The white circles are centered on the DR21(OH) clump and indicate radii of 0.5, 1.5, 3, and 4 pc at a distance of 1.4 kpc, which will provide reference for the virial analysis presented in Section 4. Middle right: the red box outlines the area that we use from the available SOFIA [C II] observations that cover a significantly larger region in Cygnus X North (Schneider et al. 2023). The nomenclature indicated for subfilaments is adopted from Schneider et al. (2010) and Hennemann et al. (2012): N (north), F1N, F1S, F3N, F3S, SW (southwest), S (south). Bottom and top: ^{13}CO (1−0), $C^{18}O$ (1−0), HCO^+ (1−0), $H^{13}CO^+$ (1−0), and [C II] spectra from the locations indicated in the middle left panel.

Galactic high-mass star-forming regions (Schneider et al. 2020), including a part of the Cygnus X North region, in the [C II] 158 μm line and the [O I] 63 μm line. The mapping of Cygnus X North with FEEDBACK is now completed[10] and covers the DR21 cloud, the Diamond Ring (Marston et al. 2004), and the W75N molecular cloud. The data can be found on the IRSA archive with project No. 07_0077.[11] We use data that cover the DR21 cloud; see Figure 1. The observations were

---

[10] https://astro.uni-koeln.de/index.php?id=18130

[11] https://irsa.ipac.caltech.edu/applications/sofia

Table 1
Summary of the Observational Data Sets

Instrument	Species	λ (μm)	ν (GHz)	Δ v (km s^{-1})	Θ (arcsec)
		IRAM			
EMIR	^{13}CO (1−0)	2720.4	110.20	0.2	23
EMIR	C^{18}O (1−0)	2730.8	109.78	0.2	23
EMIR	HCO^{+} (1−0)	3361.3	89.19	0.2	28
EMIR	H^{13}CO^{+} (1−0)	3455.7	86.75	0.2	29
		SOFIA			
upGREAT	[C II]	157.74	1900.54	0.5	14
		JCMT			
HARP	^{12}CO 3 → 2	869.0	345.80	0.42	15

Note. For the atomic and molecular lines, the line transition wavelength (λ) and frequency (ν) are given in columns (3) and (4), respectively. The effective velocity resolution is indicated in column (5), and the angular resolution of the original data is displayed in column (6).

carried out with the dual-frequency heterodyne array upGREAT receiver (Risacher et al. 2018) in OTF mapping mode and calibrated with the GREAT pipeline (Guan et al. 2012). We used an emission-free reference position at R.A.(2000) = $20^{\rm h}39^{\rm m}48\overset{\rm s}{.}34$, decl.(2000) = $42^\circ57'39\overset{''}{.}11$. The 2 × 7-pixel low-frequency array was tuned to the [C II] 158 μm line, and the 7-pixel high-frequency array was tuned to the [O I] 63 μm line (data not used here). The beam size at 158 (63) μm is $14\overset{''}{.}1$ (6″). Here we employ [C II] data smoothed to an angular resolution of 20″ and a velocity resolution of 0.5 km s^{-1}, which results in a typical noise rms of ∼1 K per beam. In order to improve the baseline removal to reduce striping in the data cube, we employ the principal component analysis method described in Tiwari et al. (2021), Kabanovic et al. (2022), and Schneider et al. (2023). More details on the SOFIA FEEDBACK observational scheme and data reduction are found in Schneider et al. (2020).

2.3. James Clerk Maxwell Telescope Observations

With the 15-pixel HARP instrument on the James Clerk Maxwell Telescope (JCMT), a ^{12}CO (3–2) mapping of the Cygnus X North and South areas was carried out between 2007 and 2009 within the observing programs M08AU018 (PI: N. Schneider) and M07BU019 (PI: R. Simon). The observation method and reduction of this data are the same as those described in Gottschalk et al. (2012) for the pilot study, and this full data set will be presented in more detail in a forthcoming paper. The observations have a spatial resolution of 15″ and a spectral resolution of 0.42 km s^{-1}, with a noise rms of ∼0.25 K.

2.4. Herschel Observations

We employ Herschel column density maps from the Cygnus X region that were taken as part of the HOBYS[12] program. Low angular resolution (36″) column density maps are presented in Schneider et al. (2016a). The procedure for obtaining these maps is described in Hill et al. (2011, 2012). We here use column density maps at a higher spatial resolution of 18″ that makes use of the method described in Palmeirim et al. (2013). The concept is to employ a multiscale decomposition of the flux maps and assume a constant line-of-sight temperature. The final map is then constructed from the difference maps of the convolved maps at 500, 350, and 250 μm, and the temperature information from the color temperature is derived from the 160 μm/250 μm ratio.

3. Results

3.1. Spectral-line-integrated Maps

From the large variety of lines detected with the IRAM 30 m telescope we selected a subset to present in this paper, i.e., the ^{13}CO (1−0), C^{18}O (1−0), HCO^{+} (1−0), and H^{13}CO^{+} (1−0) lines, which trace both the ridge and subfilaments. A full analysis of all detected lines with the IRAM 30 m telescope is beyond the scope of this paper. Figure 2 displays the velocity-integrated maps of these four lines. The overall emission distribution of the DR21 cloud is similar to what was shown in Schneider et al. (2010), but the new maps are significantly larger. As a result, they better cover the extent of the dense subfilaments, which are best visible to the west of the DR21 ridge. Note that the coverage is not the same for all lines, which is due to different setups for the observations. From Figure 2 we see that the ^{13}CO (1−0) and HCO^{+} (1−0) emission remains well detected outside the ridge while the C^{18}O (1−0) and H^{13}CO^{+} (1−0) lines are mostly detected toward the ridge, which indicates a large concentration of mass.

Figure 3 presents the SOFIA [C II] observations. The critical density of the [C II] 158 μm line is typically only a few × 10^{3} cm^{-3} for collisions with atomic and molecular hydrogen (i.e., H and H$_2$; Goldsmith et al. 2012), and it predominantly traces the photodissociated layers at the interface between molecular cloud and ionized phase (Hollenbach & Tielens 1999). It thus nicely complements the CO/HCO^{+} observations, as it should trace the lower-density gas. The [C II] line-integrated intensity map in Figure 3 reveals interesting differences compared to the IRAM molecular line data. Emission is detected toward the dense subfilaments that are also seen in ^{13}CO (1−0), HCO^{+} (1−0), and ^{12}CO (3–2) (see Appendix A), which have typical critical densities of ∼2 × 10^{3} cm^{-3}, 5 × 10^{4} cm^{-3}, and 3 × 10^{4} cm^{-3}, respectively (Shirley 2015). However, [C II] also traces the lower-density gas surrounding the DR21 ridge and dense subfilaments. The [C II] observations thus unveil a significant mass reservoir that is not located in the ridge and the subfilaments. This gas has a typical Herschel column density ($N_{\rm H_2}$) between 5 × 10^{21} cm^{-2} and 3 × 10^{22} cm^{-2} after correction for a ∼5 × 10^{21} cm^{-2} background (Schneider et al. 2016a, 2022). Even though [C II] is detected toward these higher column densities ($N_{\rm H_2} > 10^{22}$ cm^{-2}), these also start to be detected in CO lines (see Appendix B), which indicates that [C II] does not trace the full column density range there. Assuming that the cloud has a thickness[13] of 1–3 pc indicates that [C II] in the DR21 cloud might trace a density range between $n_{\rm H_2} = (0.5–1.6) \times 10^3$ cm^{-3} and $n_{\rm H_2} = (0.3–1.0) \times 10^4$ cm^{-3} toward the DR21 cloud. In a later paragraph we will further constrain the typical density traced by [C II]. Only at the location of the DR21 radio continuum source is there a strong peak of [C II] emission in the ridge. DR21 is the most evolved region in the ridge and a site of massive star formation with several compact H II regions and a number of possible O stars,

---

[12] Herschel imaging survey of OB young stellar objects (Motte et al. 2010).

[13] This is similar to the size in the plane of the sky or assumes that it has a slightly flattened morphology.

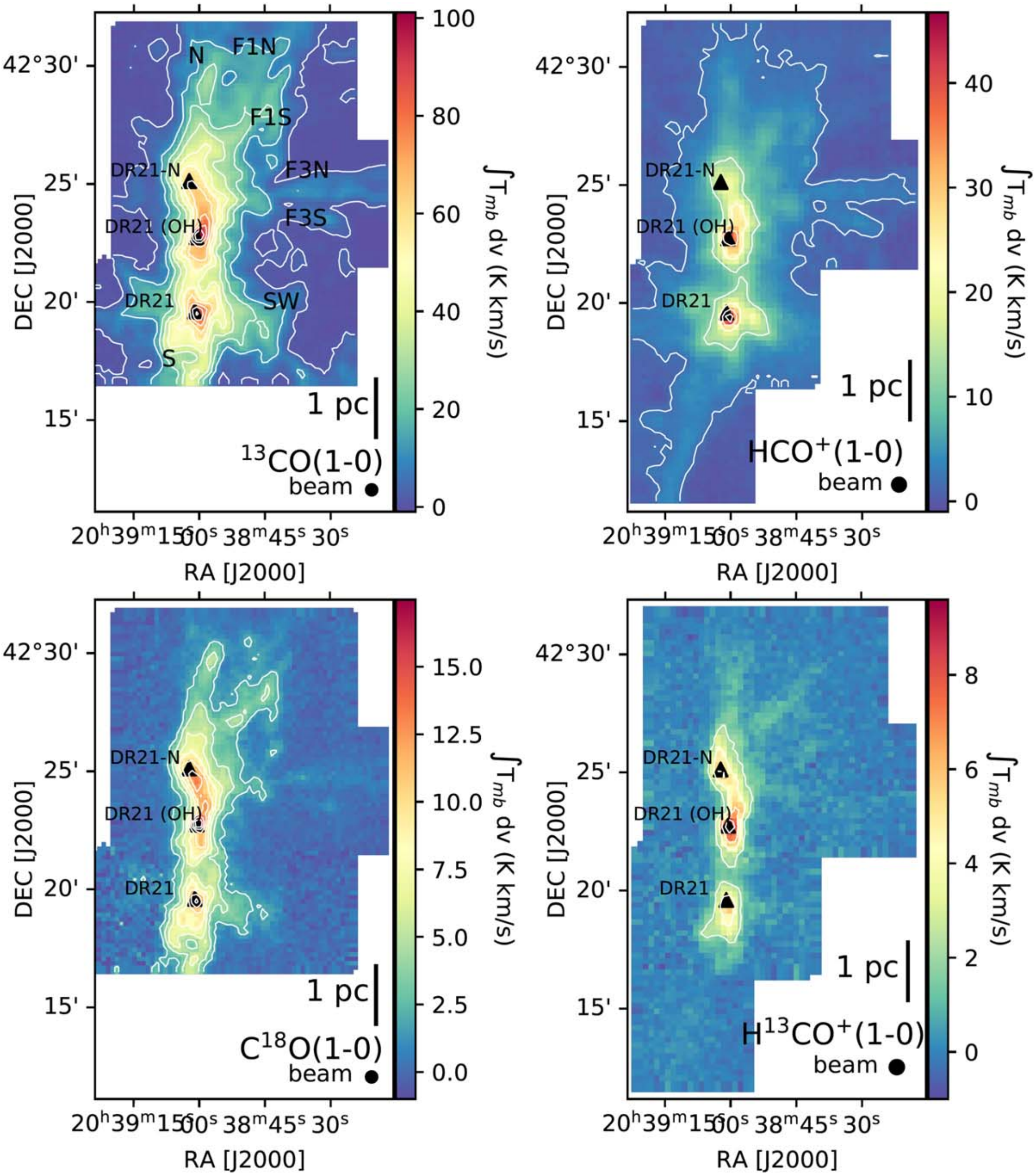

Figure 2. Top left: integrated brightness map of ^{13}CO (1−0) from −8 to 1 km s^{-1} toward the DR21 cloud. Overlaid on the map are the integrated intensity contours starting at 2 K km s^{-1} with increments of 10 K km s^{-1}. The locations of the DR21 radio continuum source (Downes & Rinehart 1966) and the DR21(OH) and DR21-N massive clumps (e.g., Motte et al. 2007) are indicated with black triangles. The subfilaments in the cloud are indicated with their names. Top right: same as the top left panel, but for HCO$^+$ (1−0) with increments of 5 K km s^{-1}. The triangles indicating DR21, DR21(OH), and DR21-N help to compare with the ^{13}CO and C^{18}O maps, from setup 2, which have a different map size. Bottom left: same as the top left panel, but for C^{18}O (1−0), with contour increments of 2 K km s^{-1}. Bottom right: same as the top left panel, but for H^{13}CO$^+$ (1−0), with contour increments of 2 K km s^{-1}.

including a prominent outflow source (Marston et al. 2004). Stellar winds (Cyganowski et al. 2003; Immer et al. 2014) probably dominate the dynamics of that region. As the [C II] emission in the DR21 source is strongly affected by the local feedback from the embedded O stars, this region is mostly left out for the work presented in this paper. Lastly, we also note from Figure 3 that the [C II] emission unveils filamentary gas to the east of the ridge that is not detected with Herschel or molecular line data. This is probably because of the low contrast with the significant Herschel column density background and because these filamentary structures are not visible in molecular line data.

3.2. Spectra and Channel Maps

The average spectrum for the entire DR21 ridge is presented in Figure 4, which shows multiple velocity components in the velocity range between −10 and 20 km s^{-1}. In this paper we will exclusively focus on the emission between −8 and 1 km s^{-1}, highlighted in Figure 4, which is the emission originating from the DR21 cloud (Schneider et al. 2006, 2010). The components of the full spectrum are discussed in Schneider et al. (2023).

The channel maps of ^{13}CO (1−0) emission, shown in Figure 5, resolve the velocity structure in the DR21 cloud. The

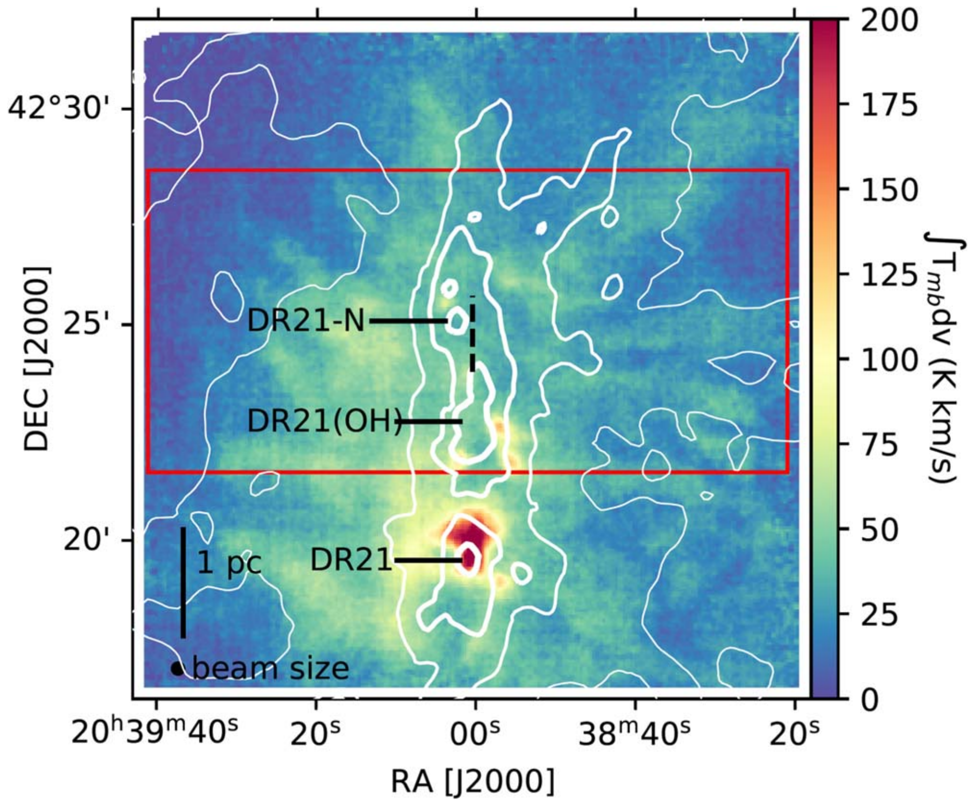

Figure 3. Line-integrated emission from −8 to 1 km s^{-1} for [C II]. The [C II] emission shows that there is extended emission around the ridge and subfilaments. The white contours indicate the Herschel column density map at $N_{\mathrm{H_2}} = 10^{22}$ cm^{-2}, 3×10^{22} cm^{-2}, 10^{23} cm^{-2}, and 4×10^{23} cm^{-2}. The red box outlines the area used to make the PV diagram perpendicular to the DR21 ridge in Figure 10. The vertical dashed black line defines the center ($r = 0$ pc) used for the PV diagram. The locations of the DR21 radio continuum source (Downes & Rinehart 1966) and the DR21(OH) and DR21-N massive clumps (e.g., Motte et al. 2007) are indicated.

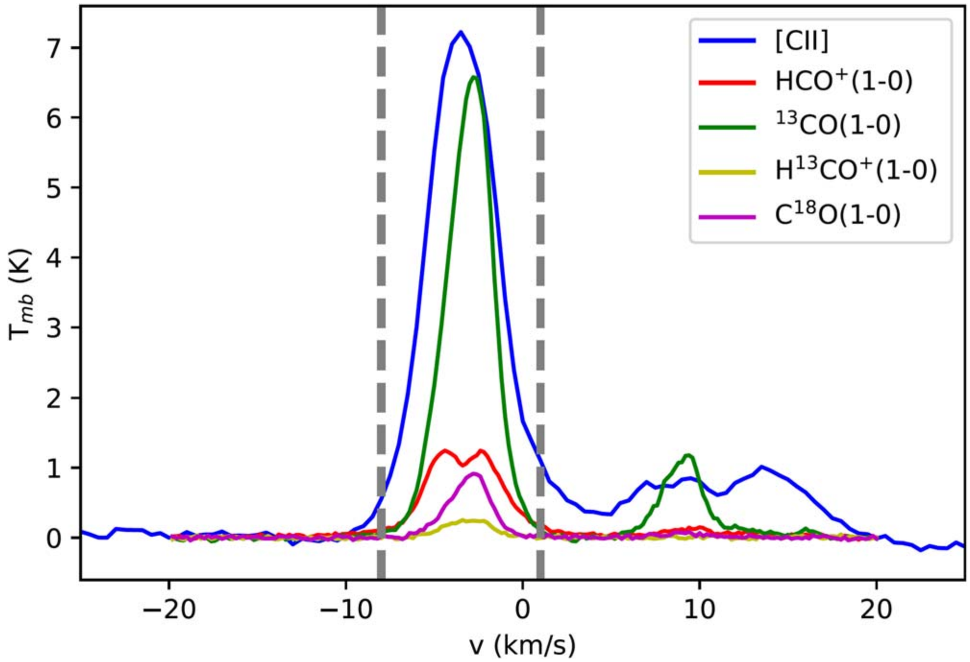

Figure 4. Average spectrum of the DR21 ridge (excluding the DR21 continuum source) displaying multiple velocity components between −10 and 20 km s^{-1}. The focus of this paper is on the emission between −8 and 1 km s^{-1} alone, indicated by the dashed vertical lines, which is the velocity range associated with the DR21 ridge (Schneider et al. 2006, 2010).

emission in the velocity range from −5 to −2.5 km s^{-1} is organized in a north–south elongated coherent structure mostly inside the $N_{\mathrm{H_2}} = 10^{23}$ cm^{-2} dust column density contour and forms the ridge. In this velocity range, the channel maps show a north–south velocity gradient in the ridge. At higher and lower velocities inside the ridge, the emission is more clumpy and concentrates on the DR21(OH) and DR21 locations. At velocities between −4 and −2.5 km s^{-1} the subfilament F1S

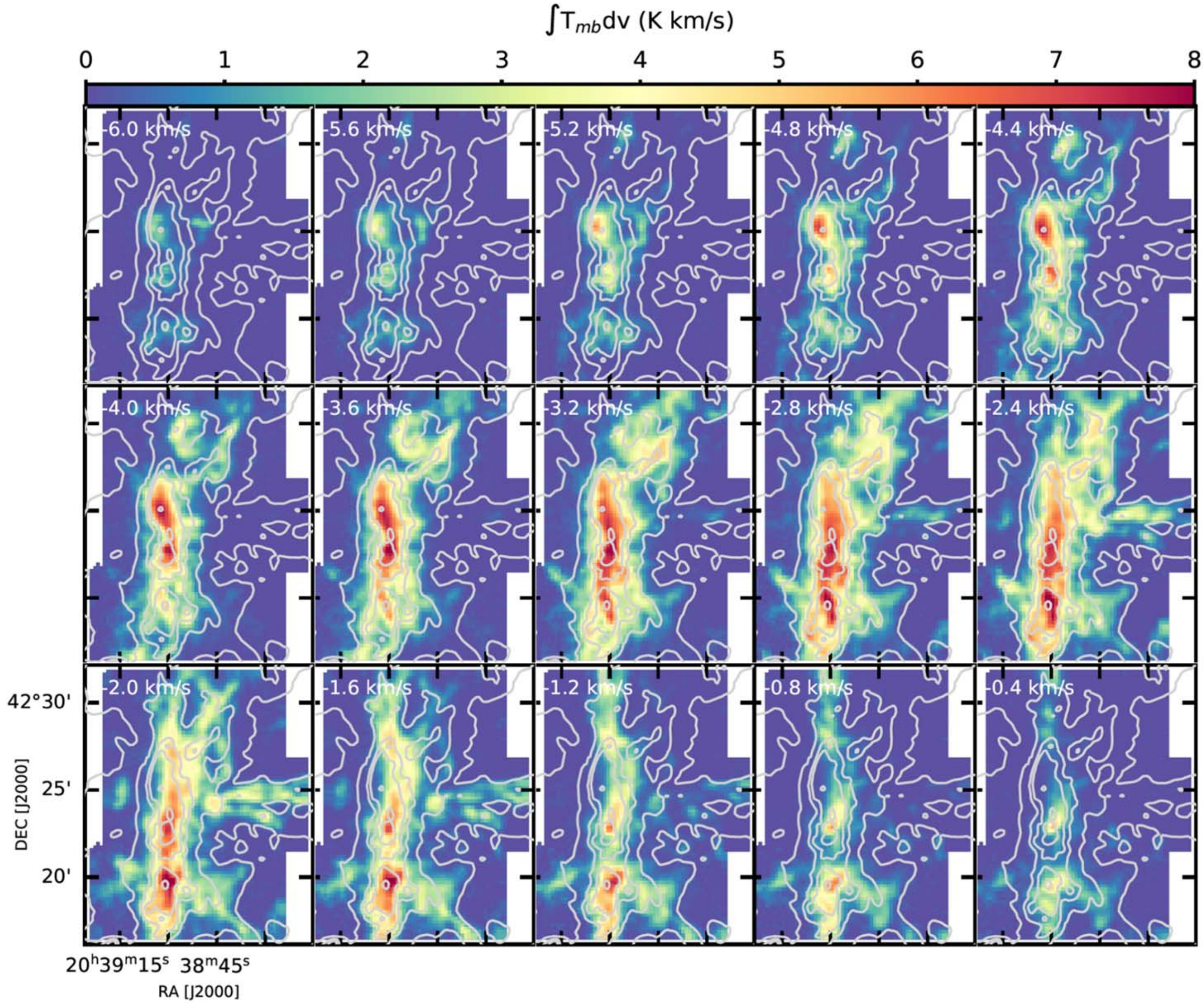

Figure 5. ^{13}CO (1−0) channel maps (IRAM) between −6.0 and −0.4 km s^{-1} of the DR21 cloud. The gray contours trace the Herschel column density at $N_{\mathrm{H}_2} = 10^{22}$ cm^{-2}, 2×10^{22} cm^{-2}, 5×10^{22} cm^{-2}, 10^{23} cm^{-2}, and 5×10^{23} cm^{-2}, to highlight the ridge and subfilaments. Most subfilaments become particularly visible at $v_{\mathrm{lsr}} > -3$ km s^{-1}.

becomes visible, and between −3 km s^{-1} and −1 km s^{-1} all the other western subfilaments become prominent.

Inspecting the ^{13}CO (1−0), C^{18}O (1−0), HCO^{+} (1−0), H^{13}CO^{+} (1−0), and [C II] spectra over the map in Figure 1, we find that the spectra show skewed profiles. This is also the case for H^{13}CO^{+} (1−0) and C^{18}O (1−0), which are optically thin for excitation temperatures in the DR21 ridge down to 10 K. This suggests the presence of multiple components, which we will address later on. The selected positions in Figure 1 represent typical lines in the ridge (positions 1, 2, 3, and 5) and in the subfilaments (positions 4 and 6). Note that the HCO^{+} (1−0) spectra in the ridge display strong self-absorption centered on the velocities of peak emission for C^{18}O (1−0) and H^{13}CO^{+} (1−0); see Schneider et al. (2010) for more discussion. Furthermore, it becomes obvious in Figure 1 that HCO^{+} (1−0) has high-velocity wing emission toward DR21 and DR21(OH), tracing the prominent molecular outflows in these regions.

The [C II] spectra also show flat-topped and skewed line profiles in Figure 1. Since some bright [C II] regions were found to experience [C II] self-absorption and optical depth effects (Graf et al. 2012; Guevara et al. 2020; Kabanovic et al. 2022), we verified whether this could be the case for the DR21 ridge. The [C II] spectra do not show a noteworthy dip, seen for HCO^{+} (1−0), which argues against self-absorption. In Appendix C, the optical depth of the [C II] line is calculated using the [^{13}C II] noise level, which indicates a maximal optical depth of $\tau = 1.7$. In addition, we performed calculations with RADEX (van der Tak et al. 2007), which indicates that the optical depth for [C II] typically is below 1 for the DR21 cloud. The [C II] line shape is thus not caused by optical depth effects but rather by multiple velocity components around the DR21 ridge. This also fits with the observation in Figure 4 that the peak [C II] emission is displaced from the peak molecular line emission. Therefore, we fit the spectra with multiple Gaussian velocity components (see Appendix D) over the full map and analyze the goodness of the fit with the Beyond The Spectrum (BTS) fitting algorithm (Clarke et al. 2018). We find that the [C II] emission in the range of −8 to 1 km s^{-1} consists of either one or two velocity components that are typically separated by ∼2–3 km s^{-1}. The first component is typically around −4.5 km s^{-1}, and the second one is typically around −2.5 km s^{-1} (see Figure 21 in Appendix D). The fitting results of Figure 19 in Appendix D also show that the regions with multiple velocity components are concentrated in the close vicinity of the DR21 ridge.

3.3. The Velocity Field of the DR21 Cloud

Even though the spectra are slightly more complex than a single Gaussian in the −8 to 1 km s^{-1} velocity range, we performed a single Gaussian line fitting on the data sets to obtain information on the global velocity distribution and line width for the different tracers. A fit was accepted when the brightness was higher than 3× the noise rms in the different tracers. Note that moment maps might be better suited to give a view on the global dynamics in the region. However, in large regions of the observed map the signal-to-noise ratio (S/N) of the data is not abundant, while excellent S/N is required for producing trustworthy moment maps (e.g., Teague 2019). As a result, the produced first and second moment maps have large uncertainties in the subfilaments and do not provide a good visualization of the velocity field there.

The resulting velocity maps for the molecular lines are presented in Figure 6 and show similar velocity gradients over the ridge to the ones presented in Schneider et al. (2010) using only N_2H^+ (1–0). We confirm that there is not a single gradient perpendicular to the ridge, but that the velocity pattern over the ridge shows organized velocity gradients with altering orientation. These altering velocity gradients are mixed with a clear north–south velocity gradient from −4.5 to −2.5 km s^{-1}. Remarkably, the velocities of the subfilaments (N, F1N, F3N, F3S, and SW) in all lines are redshifted ($v_{\rm LSR}$ ∼ −2.5 to −1 km s^{-1}) with respect to the ridge (bulk emission around −3.5 km s^{-1}). Only the F1S subfilament at velocities around −3.5 km s^{-1} is not significantly redshifted with respect to the ridge but is not blueshifted either. Lastly, the southern subfilament appears slightly redshifted close to the ridge, but more to the south this filament becomes less redshifted with respect to the ridge. This observation of dominantly redshifted subfilaments and a complete lack of a truly blueshifted subfilament with respect to the ridge is noteworthy and confirms the observations in the channel maps of ^{13}CO (1−0) in Figure 5.

The [C II] observations trace the lower-density gas kinematics in the cloud and thus provide a complementary view on the surrounding gas kinematics in the cloud off the dense filamentary structures. The velocity field is shown in Figure 7. There is, similar to the molecular line observations, mostly systematically redshifted emission ($v \sim -3$ to −1 km s^{-1}) in the cloud around the ridge. This redshifted gas becomes increasingly prominent farther away from the ridge. In addition, Appendices D and E show that there is an excellent correspondence in velocity of the subfilaments and this redshifted [C II] emission, indicating that the subfilaments are directly embedded in this mass reservoir seen with [C II]. However, the [C II] velocity field also shows additional features. In particular, blueshifted velocities down to $v = -5$ km s^{-1} are found in localized regions directly east and northwest of the ridge. No blueshifted gas is found farther away from the ridge and the F1S filament. This fits with the observation in Figure 4 that the average [C II] emission has an offset from the molecular line emission and that it is associated with the presence of two [C II] velocity components (at −4.5 and −2.5 km s^{-1}) established in the previous section. Lastly, from Figure 20 in Appendix D we also note that these regions with more blueshifted velocities overlap with the regions that have two fitted velocity components. In these regions the blueshifted velocity component is thus the dominant source of emission that affects the observed velocity field.

3.4. Line Widths

The Gaussian line fitting also provides maps of the FWHM for the spectra. The results for the optically thinner lines $C^{18}O$ (1−0) and $H^{13}CO^+$ (1−0) are presented in Figure 8. The $C^{18}O$ (1−0) map indicates, where detected, that the subfilaments have a lower FWHM than the ridge, typically $\lesssim$1 km s^{-1}. In the ridge, a FWHM between 1 and 2.5 km s^{-1} is observed (which typically has two velocity components; see Appendix E). Noteworthy is the strong local increase of the FWHM up to 4 km s^{-1} at locations where the subfilaments connect to the ridge. This behavior is also observed in the velocity dispersion maps of N_2H^+ (1–0) (Schneider et al. 2010) and NH_3 (Keown et al. 2019). One would expect that this is the result of overlapping velocity components, associated with the subfilament and the ridge, at this connection. However, Appendix E shows that these regions are best fitted with a single Gaussian component. This suggests either that the overlapping velocity components are closely blended together or that there is a rapid change in the line-of-sight velocity field at the edge of the ridge, for example, due to accretion shocks.

Comparing the FWHM maps for the molecular lines in Figure 8 with those of the [C II] line, we observe three clear differences. First, the [C II] line has a significantly larger line width (typically > 4–5 km s^{-1}) than the molecular lines over the full map. Note that the largest FWHMs are associated with the DR21 outflow, which is not the focus of our study. Second, the highest [C II] FWHM values, excluding the DR21 outflow, are found outside of the dense DR21 ridge, mostly in the eastern region without molecular dense subfilaments. This east–west asymmetry with respect to the ridge for the [C II] line width is remarkable and seems to be correlated with the lack of dense subfilaments east of the ridge. Third, examining the map in more detail, it is also observed that the [C II] emission directly surrounding the subfilaments has a significantly larger line width than the emission toward the subfilaments. In Figure 1, it is observed that this broader [C II] line width is the result of the flat-topped spectra, which are due to more blueshifted [C II] emission with respect to the molecular lines. This more blueshifted [C II] emission is the result of the prominent blueshifted [C II] velocity component found in Appendix D and thus is not necessarily the result of higher turbulent support. This demonstrates that the molecular lines miss an important part of the picture to understand the full DR21 molecular cloud dynamics and evolution.

4. Analysis

4.1. The C^+ Column Density and Excitation

In Section 3.1, it was estimated that [C II] traces gas between 5×10^2 cm^{-3} and 10^4 cm^{-3}. Here we will explore the excitation conditions and regions traced by the [C II] emission

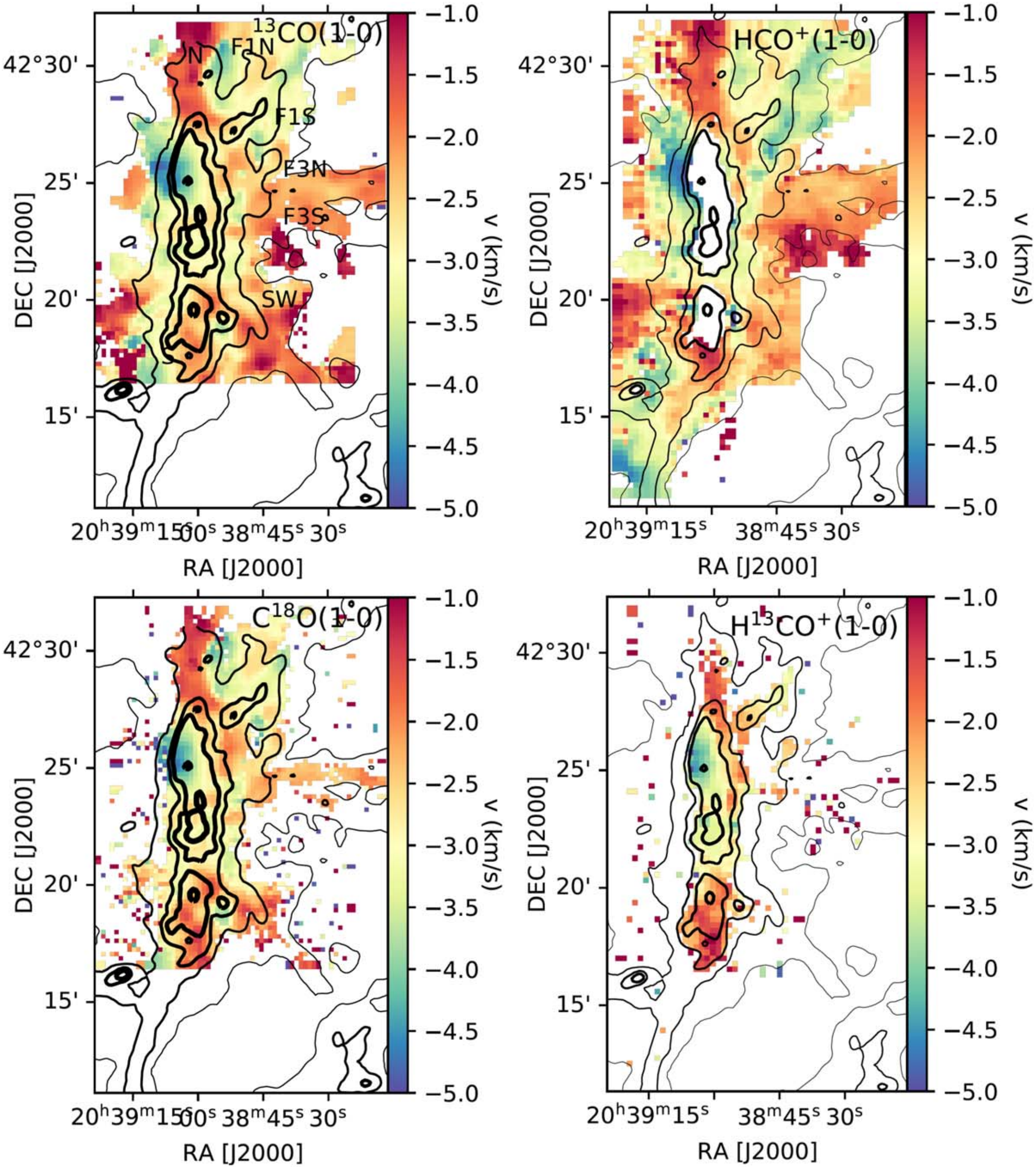

Figure 6. Top left: velocity map of ^{13}CO (1−0) over the DR21 ridge and subfilaments, obtained from fitting a single Gaussian to the spectra. The uncertainty of the centroid velocity is below 0.15 km s^{-1} over the entire map. Overplotted on the map are the Herschel column density contours at $N_{\rm H_2} = 10^{22}$ cm^{-2}, 2×10^{22} cm^{-2}, 5×10^{22} cm^{-2}, 10^{23} cm^{-2}, and 5×10^{23} cm^{-2}, which indicate the ridge and the surrounding subfilaments. The subfilaments are indicated with their name from Hennemann et al. (2012). Top right: same as the top left panel, but for HCO$^+$ (1−0) without fitting inside the DR21 ridge because of the HCO$^+$ (1−0) self-absorption there. Bottom left: same as the top left panel, but for C^{18}O (1−0). Bottom right: same as the top left panel, but for H^{13}CO$^+$.

in more detail. To determine the typical temperature of the C$^+$ gas, we consider the heating from far-UV (FUV) photons. From the FUV field map calculated in Schneider et al. (2016b), we find that the DR21 cloud is located in an FUV field up to $G_0 = 200$–400 Habing owing to heating from the local UV source in the region (see also Schneider et al. 2023). This fits with the typical line-integrated [C II] intensity toward the surrounding cloud of ∼50 K km s^{-1}, which is expected for an FUV field of $G_0 = 200$ Habing in the PDR Toolbox (Kaufman et al. 2006; Pound & Wolfire 2008, 2023) at densities between 5×10^2 cm^{-3} and 10^4 cm^{-3}. For this FUV field strength and density range, the PDR Toolbox predicts temperatures of 100–200 K for the [C II]-emitting gas of the photodissociation region (PDR).

With these excitation conditions, it is possible to produce the C$^+$ column density map over the full extent of the FEEDBACK map using the equation from Goldsmith et al. (2012),

$$\Delta T_A = 3.43 \times 10^{-16} \times \left[1 + 0.5e^{91.25/T_{\rm kin}}\left(1 + \frac{2.4 \times 10^{-6}}{C_{\rm ul}}\right)\right]^{-1} \frac{N({\rm C}^+)}{\delta v}, \quad (1)$$

with ΔT_A the brightness temperature for a uniform source that fills the beam, $T_{\rm kin}$ the kinetic temperature, $C_{\rm ul}$ the collisional

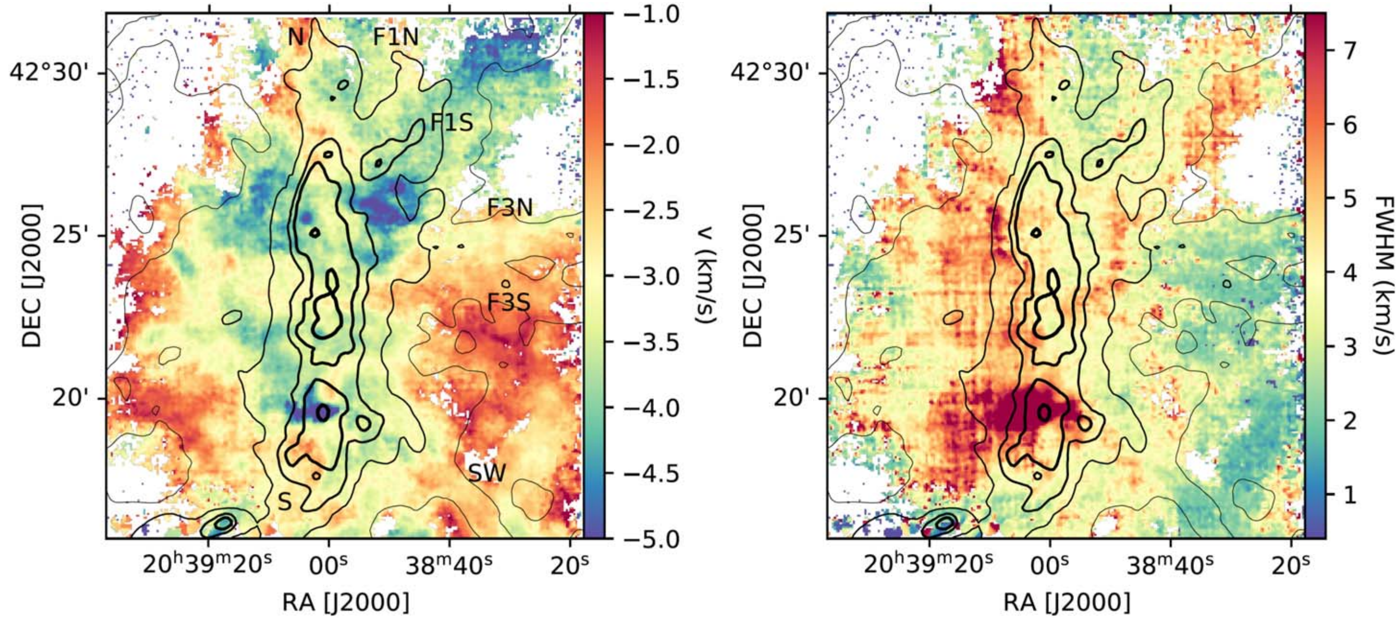

Figure 7. Left: velocity field observed with [C II]. The black contours indicate the Herschel column density contours at $N_{H_2} = 10^{22}$ cm^{-2}, 2×10^{22} cm^{-2}, 5×10^{22} cm^{-2}, 10^{23} cm^{-2}, and 5×10^{23} cm^{-2}. The subfilaments are indicated with their name. Right: same as the left panel, but for the [C II] FWHM.

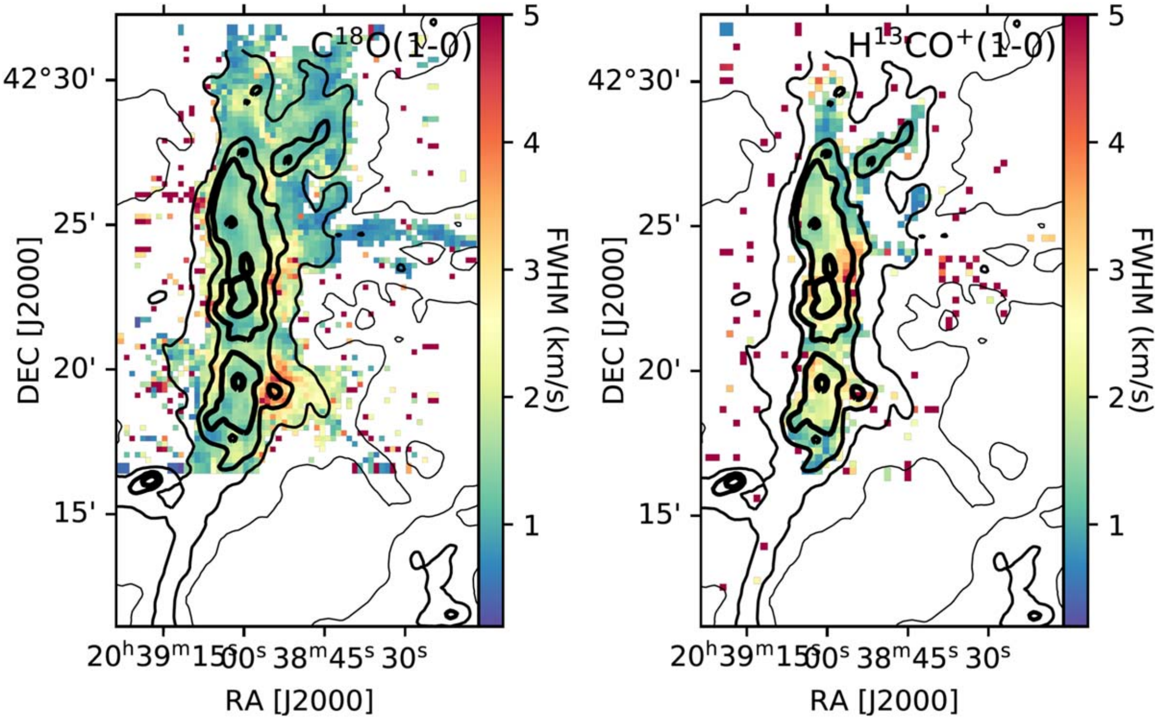

Figure 8. Left: FWHM map of $C^{18}O$ (1−0) over the DR21 ridge and subfilaments. The uncertainty of the FWHM is generally below 0.1 km s^{-1} and always below 0.4 km s^{-1} over the entire map. Overplotted on the map are the Herschel column density contours at $N_{H_2} = 10^{22}$ cm^{-2}, 2×10^{22} cm^{-2}, 5×10^{22} cm^{-2}, 10^{23} cm^{-2}, and 5×10^{23} cm^{-2}. Right: same as the left panel, but for $H^{13}CO^+$ (1−0).

deexcitation rate, $N(C^+)$ the C^+ column density, and δv the line width. C_{ul} is given by

$$C_{ul} = n \times R_{ul}, \tag{2}$$

where R_{ul} is the deexcitation rate coefficient given by

$$R_{ul} = 3.8 \times 10^{-10}\, \mathrm{cm^3\, s^{-1}} (T_{kin}/100)^{0.14}. \tag{3}$$

Using a $T_{kin} = 100$ K and $n_{H_2} = 5 \times 10^3$ cm^{-3} then gives C^+ column densities $N(C^+) \approx (0.4–1.0) \times 10^{18}$ cm^{-2} over the extent of the cloud, which is shown in Figure 9. However, note that these assumed excitation conditions are not valid for the DR21 radio continuum region, as it is a dense and strongly irradiated PDR. Comparing this C^+ column density map with the deduced H_2 column density map from the Herschel data also allows us to estimate the $[C^+]/[H_2]$ abundance ratio over the map. This shows that we find a C^+ abundance around 10^{-4} in the outer parts of the cloud around the ridge and subfilaments, which is of the order of the elemental abundance

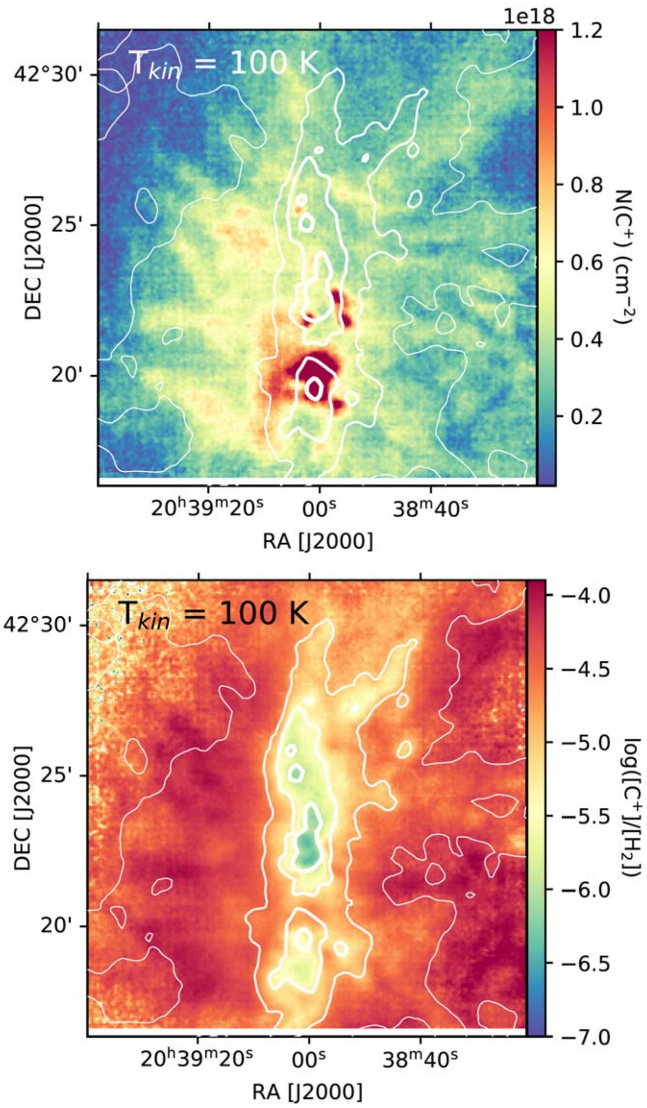

Figure 9. Top: C^+ column density map between −8 and 1 km s^{-1} assuming a kinetic temperature of 100 K and $n_{H_2} = 5 \times 10^3$ cm^{-3} for the excitation conditions. Note that these excitation conditions, which should be representative for most of the map, are most likely not valid toward the peak around the DR21 radio continuum region in the south of the map, as this region experiences strong internal heating. Bottom: the resulting $[C^+]/[H_2]$ abundance ratio deduced from the Herschel column density map over the DR21 cloud on a log scale.

ratio of carbon (χ_C) in the ISM (e.g., Glover & Clark 2012). Basically all carbon is thus found in the ionized state (C^+) in these regions. Toward the subfilaments, we find under these conditions that ∼10% of the gas is traced by [C II], and toward the ridge this drops even lower to values between 0.1% and 1%. We do, however, note that the density and temperature are an important assumption. A higher temperature up to 200 K can reduce the C^+ column density by ∼50%, while a lower temperature can increase the C^+ column density by a factor 2. A lower typical density of 10^3 cm^{-3} can increase the column density by an additional factor 2. However, such a $N(C^+)$ increase due to a low density would result in a C^+ abundance above the elemental abundance. This suggests that a significant part of the [C II] emission originates from regions with a typical density of $n_{H_2} \sim 5 \times 10^3$ cm^{-3}. Combining this density with the Herschel column density for the surrounding clouds results in a maximal line-of-sight depth of 2 pc. This implies that the surrounding cloud of the DR21 ridge has a sheet-like morphology.

The same analysis is done for ^{13}CO (1−0) in Appendix B. This analysis indicates that the ^{13}CO abundance peaks in some subfilaments and at the edges of the DR21 ridge. The abundance then decreases in the ridge and in the outer cloud. In both the ridge and the outer part of the cloud, ^{13}CO (1−0) appears to trace only a fraction of the total gas mass. Combined, this provides compelling evidence that [C II] indeed traces most of the surrounding gas in the DR21 cloud. The regions surrounding the ridge and subfilaments are thus CO-poor gas that lights up in [C II]. In combination with the molecular line data, [C II] thus provides a global view of the cloud.

4.2. Position–Velocity Diagram of the Ridge

The position–velocity (PV) diagram perpendicular to the DR21 ridge gives an additional view on the cloud kinematics with respect to the ridge. Figure 10 shows PV diagrams for the optically thick (HCO^+ (1−0) and ^{12}CO (3–2)) and thin ($H^{13}CO^+$ (1−0) and $C^{18}O$ (1−0)) molecular lines observed with the IRAM 30 m and JCMT (see the red box in Figure 3 for the covered region). It confirms that the emission from subfilaments outside the ridge is at more redshifted velocities with respect to the densest gas in the ridge. This gives rise to a V-like shape in the PV diagram, similar to what was observed for the Musca filament (Bonne et al. 2020a), which has about the same size as the DR21 ridge but has a mass that is two orders of magnitude lower. For the Musca filament this was proposed to be the result of magnetic field bending by the interaction of an overdensity with a more diffuse region in the colliding H I cloud. As for this previous study of the low-mass Musca filament, the DR21 ridge is located at the apex of this V-like shape. However, the V shape for DR21 in molecular lines is not as clear as the ones observed in Musca. This can be related to the rapid line width increase within 1 pc of the DR21 ridge, while the Musca filament is transonic (Hacar et al. 2016; Bonne et al. 2020a). Such a rapid line width increase in the densest regions is predicted to be the result of parsec-scale gravitational acceleration in massive clouds (e.g., Peretto et al. 2006, 2007; Hartmann & Burkert 2007; Gómez & Vázquez-Semadeni 2014; Watkins et al. 2019) and could also be the result of accretion-driven turbulence (Klessen & Hennebelle 2010). A gravitational collapse scenario is also supported by the strong blue asymmetry self-absorption of HCO^+ (1−0) that covers the same velocity interval as the perpendicular velocity gradients over the ridge (Schneider et al. 2010).

Figure 10 also presents the [C II] PV diagram, which traces the surrounding gas in the DR21 cloud. The PV diagram shows that the surrounding gas forms a redshifted V shape perpendicular to the DR21 ridge on large scales ($|r| > 1$ pc). The Pearson correlation coefficients for the central [C II] velocity as a function of radius are −0.76 and 0.89 on the east and west side of the ridge, respectively. With bootstrapping we find that these coefficients are far out of the 95% intervals for the null hypothesis that there is no correlation, i.e., [−0.19, 0.20] (east) and [−0.18, 0.17] (west), and thus demonstrate a clearly organized velocity field perpendicular to the ridge. As the cloud appears to be organized in a sheet, this points at a curved sheet. However, in [C II] it is also observed that there

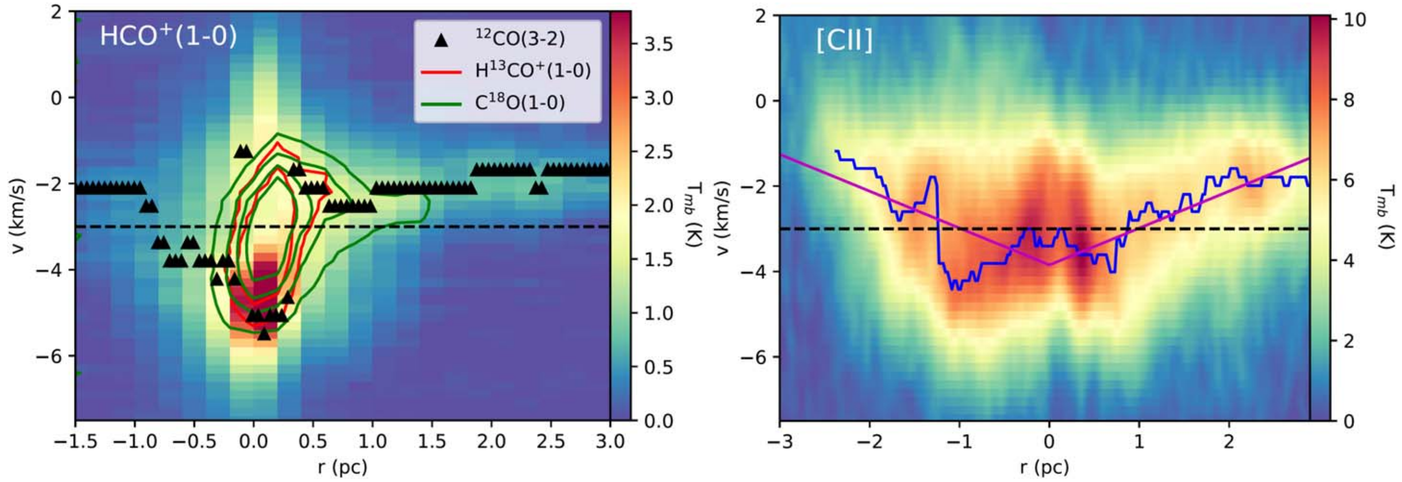

Figure 10. Left: HCO$^+$ (1−0) PV diagram, with the green and red contours indicating the emission from C^{18}O (1−0) and H^{13}CO$^+$ (1−0), respectively. The PV diagram was constructed perpendicular to the filament from the region indicated by the red box in Figure 3 by averaging the intensities along the declination axis in this box. The black triangles follow the peak brightness velocity of ^{12}CO (3–2) as a function of the distance (r) from the center of the ridge. This indicates that the gas is redshifted at both sides of the ridge, which is at a velocity of ∼−3 km s^{-1} (indicated by the dashed horizontal line). At the ridge, there is a large increase in line width, associated with the velocity gradients observed over the ridge in Figure 6. This fits with the observed HCO$^+$ (1−0) blue asymmetry in the PV diagram due to self-absorption in a collapsing cloud. Right: the [C II] PV diagram perpendicular to the DR21 ridge over the same region, with the blue line following the peak brightness velocity. On large scales ($|r| > 1$ pc), the [C II] emission shows a redshifted V shape followed by a sharp transition to more blueshifted emission at $|r| < 1$ pc, which makes the velocity profile deviate from a pure V shape. To highlight this, we fitted a V shape to the PV diagram, which is indicated in magenta. We interpret this to be due to a second, more spatially concentrated velocity component that is associated with the formation of the DR21 ridge. The Pearson coefficients for the central velocity as a function of radius are −0.76 and 0.89 on the east and west side of the ridge, respectively. This points to a relatively well organized, but not perfect, correlation for the central velocity with radius.

are deviations from a pure V shape due to blueshifted emission in the vicinity of the ridge at $|r| \sim 1$ pc. This deviation from the V shape is particularly visualized in the PV diagram by the sharp peak velocity transition at $|r| \sim 1$ pc and might explain why the Pearson correlation coefficients are not equal to 1. We propose that this traces two distinct but converging velocity components at −4.5 and −2.5 km s^{-1} in the DR21 cloud that drive continuous mass inflow to the DR21 ridge, which is located at the intersection of these flows.

4.3. Convergence of Blue- and Redshifted Gas in the DR21 Cloud

The molecular line observations demonstrated the existence of an organized velocity field over the ridge, similar to the results presented in Schneider et al. (2010). This internal velocity field is proposed to be connected to the inflowing subfilaments in the surrounding cloud and is typically considered to be tracing inflow. Using 8 μm observations from the Spitzer Space Telescope (Hora et al. 2009), we attempt to portray a 3D configuration of the ridge and subfilaments. Inspecting the 8 μm map of the DR21 cloud (Figure 11), it becomes obvious that heavily reduced 8 μm emission (“IR-dark”) traces regions inside the ridge, except for the bright compact sources at DR21 and DR21(OH), which show internal regions heated by stellar/young stellar object feedback. Consequently, this indicates that the gas associated with strong 8 μm extinction is located at the front side of the DR21 ridge with $N_{\mathrm{H}_2} > 10^{23}$ cm^{-2}, as this is a foreground layer absorbing 8 μm emission. The region of the ridge with more extended 8 μm emission is then located toward the back of the DR21 ridge. Toward the subfilaments similar, but lower contrast, 8 μm extinction is observed. The overlay of the 8 μm map with contours of molecular and [C II] line emission at $v = -4.6$ and −1.6 km s^{-1} indicates that the most blueshifted molecular line emission corresponds to the extended 8 μm emission features, while the redshifted line emission corresponds to the darkest 8 μm regions. This clearly indicates that the redshifted gas is located in front of the blueshifted gas from our point of view, which confirms that the flows in the ridge and cloud are indeed converging. The red- and blueshifted velocity components that make the V shape in the PV diagram are thus accreted on the ridge. Note that there are several contaminants (DR21, protostellar objects, etc.), a lower contrast, and a more complex contour distribution that make the [C II] map less straightforward to evaluate. Nonetheless, there is a clear association at several locations between the distribution of the redshifted gas and 8 μm extinction in the surrounding cloud that is traced by this line.

4.4. Virial Analysis of the DR21 Cloud

In Schneider et al. (2010) it was found that the DR21 ridge is gravitationally collapsing. With the newly obtained data sets, we can further investigate the global stability of the molecular cloud as a function of its radius, centered on the column density peak in DR21(OH). This is done with the different tracers by estimating the gravitational potential energy, the turbulent energy, and the magnetic energy. In this analysis, the density profile of the cloud might affect the results that use the simple equations below, which correspond to a sphere with uniform density. The same is valid for the more sheet-like morphology that we propose for the surrounding DR21 cloud to maintain a plausible C$^+$ abundance. However, the impact of these differences from a uniform sphere are predicted to be relatively small ($\lesssim$50% for typical clump density profiles and a not too flattened ellipsoid cloud based on Bertoldi & McKee 1992). Therefore, considering the uncertainties, we think that the analysis below is reasonable. The thermal and turbulent energy

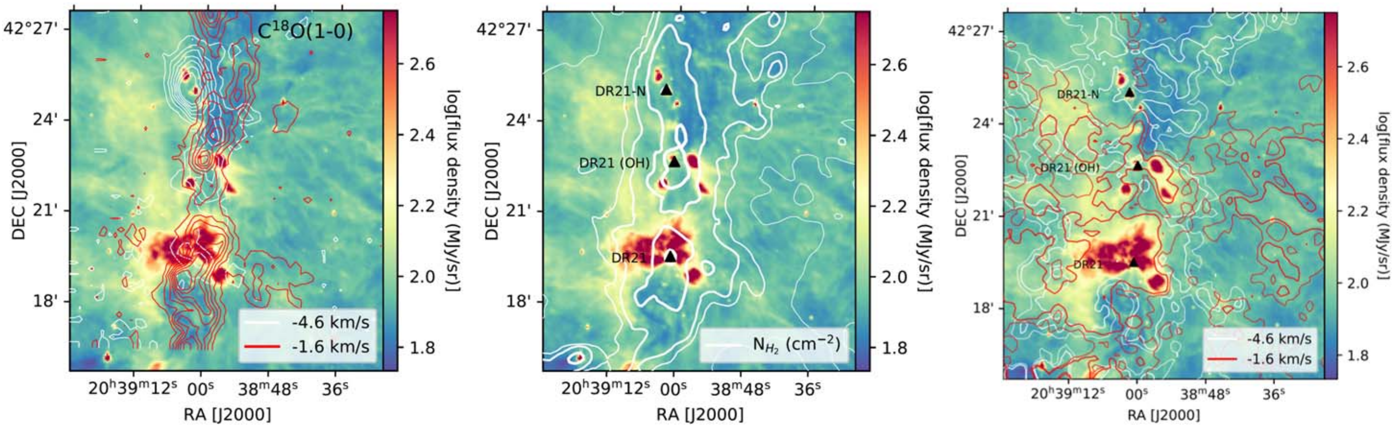

Figure 11. Spitzer 8 μm image of the DR21 cloud overlaid with velocity contours of C^{18}O (1−0) (left) and [C II] (right) at −1.6 and −4.6 km s^{-1}, and overlaid with the Herschel column density (middle). The northern and southern parts of the ridge show 8 μm extinction, i.e., are "IR-dark," while in the middle there is strong emission at the locations of DR21 and DR21(OH). Some protostellar sources show up as localized emission spots. Outside of the ridge, the 8 μm emission is extended and rather diffuse, with some feather-like features. The contours of C^{18}O (1−0) indicate that the more blueshifted emission is located toward the region with IR emission in the ridge, while the redshifted emission is concentrated toward the strong 8 μm extinction. The structure of the [C II] emission is more complex, as it is more diffuse and also affected by the feedback in DR21 and local protostellar sources (e.g., around DR21(OH)). However, there is overall a correspondence on the large scales of the blueshifted gas to bright Spitzer 8 μm regions and redshifted gas to 8 μm extinction. The figure in the middle indicates the location of DR21, DR21 (OH), and DR21-N for reference of their location.

is calculated using

$$E_T = \frac{3}{2} M\, \sigma^2, \tag{4}$$

with M the mass in the region determined from the Herschel dust column density map and σ the velocity dispersion of the studied region (which we approximate here with the observed line width, as there is no direct measure of the kinetic temperature). The gravitational energy is determined by

$$E_G = -\frac{3}{5}\frac{GM^2}{R}, \tag{5}$$

where G is the gravitational constant and R the radius. The magnetic energy is calculated using

$$E_{\rm mag} = \frac{1}{2} M\, V_{\rm A}^2, \tag{6}$$

with $V_{\rm A}$ the Alfvén speed, which is given by $V_{\rm A} = \frac{B}{\sqrt{\mu_0 \rho}}$, with μ_0 the vacuum permeability, ρ the density, and B the magnetic field strength.

The evolution of mass as a function of radius from DR21 (OH) is shown in Figure 12. The increase in mass flattens as a function of radius at $r > 1.5$ pc, which is expected with mass concentration in the ridge. For the error on the mass, we assume an uncertainty of 15% for the derived column density, as this corresponds to typical differences when creating the column density map with different methods (e.g., Peretto et al. 2016). To estimate the thermal and turbulent internal support of the cloud, we assume that the line widths of the observed lines, i.e., ^{13}CO (1−0), C^{18}O (1−0), H^{13}CO$^+$ (1−0), and [C II], are a good proxy. This turns out to be a good approximation, as their line width is dominated by nonthermal motion. Note that this approach ignores that a significant part of the line width might be associated with organized convergent flows driven by gravitational collapse or inertial motion instead of internal support (Traficante et al. 2018a, 2018b, 2020) and that we have demonstrated the presence of multiple velocity components associated with inflow. The line width as a function of radius for the three considered molecules is presented in Figure 12. It shows an increasing line width toward small radii and a fairly constant line width at $r > 1.5$ pc. The increasing line width toward the ridge can fit with gravitationally driven inflow. This would also fit with predictions by Traficante et al. (2020) since most of the mass in the DR21 cloud has column densities $\gg$0.1 g cm^{-2} (i.e., $N_{\rm H_2} \gg 2.6 \times 10^{22}$ cm^{-2}). The estimated kinetic support based on the line width is thus an upper limit on the turbulent support and might significantly overestimate it. We do have to note that the current IRAM 30 m does not entirely cover the studied radii, but the [C II] data showed that these regions are highly CO-poor.

Determining the magnetic field in the cloud as a function of its size is the most uncertain quantity because there are only a few dust polarization magnetic field observations in the region. Based on these observations, it was proposed in Ching et al. (2017) that the magnetic field strength in the DR21 ridge is 0.94 mG. Therefore, we used two approaches to estimate the magnetic field strength evolution in the cloud. First, we make use of the magnetic field strength relation from Crutcher et al. (2010), which is given by

$$B = \begin{cases} 0.01 \text{ mG } (n_{\rm H} < 300 \text{ cm}^{-3}) \\ 0.01 \left(\frac{n_{\rm H}}{300}\right)^{0.65} \text{ mG } (n_{\rm H} > 300 \text{ cm}^{-3}) \end{cases}. \tag{7}$$

Second, we use $B \propto n_{\rm H}^k$ and start from the constraint that the magnetic field strength is 0.94 mG at the density of the ridge. To extrapolate the relation, we use two values: $k = 0.5$ and $k = 0.67$. These exponents represent two asymptotic cases: $k = 0.67$ is generally considered to describe the case where the magnetic field is dominated by gravitational collapse, and $k = 0.5$ the case where the magnetic field plays an important role in support against gravitational collapse (e.g., Basu 1997; Hennebelle et al. 2011). The resulting magnetic field strengths as a function of radius for the different estimates are shown in Figure 12. Over the full cloud there is an uncertainty up to a factor 4 for the magnetic field strength based on the different

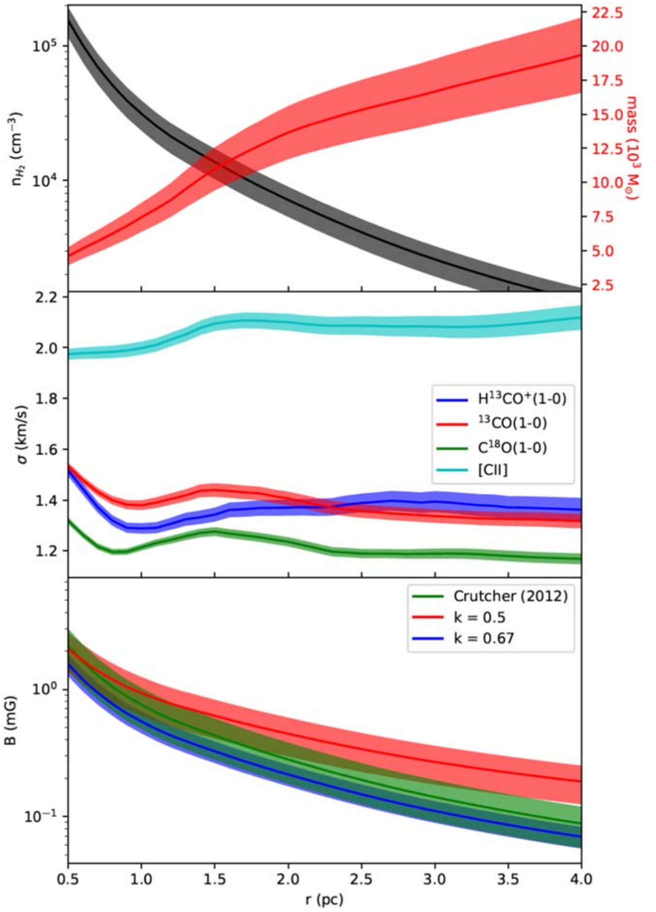

Figure 12. Top: radial profile of the average density in the DR21 cloud (in black). The average density within each radius was estimated based on the mass within the considered radius. The mass within the radius r is shown at the axis on the right (in red). Middle: same as the top panel, but for the velocity dispersion of H^{13}CO$^+$ (1−0) (in blue), ^{13}CO (1−0) (in red), C^{18}O (1−0) (in green), and [C II] (in cyan). The molecular lines show very similar behavior, while the [C II] line has a significantly higher line width. However, note that at the outer radii ($r \sim$ 3–4 pc) the cloud is not fully covered by the IRAM 30 m map (Figures 1 and 2). Bottom: estimated characteristic magnetic field strength for the gas within a radius for the three different considered profiles. The green curve shows the predictions by the Crutcher et al. (2010) relation. The red and blue curves use a magnetic field strength of 0.94 mG at the density of the ridge and $k = 0.5$ and 0.67, respectively, in $B \propto n_{\rm H}^k$.

relations used. This will thus have a significant impact on the magnetic energy as will be shown in the next paragraph.

The calculated energy terms are shown in Figures 13 and 14, compared to the gravitational energy. The thermal and kinetic energies, estimated from the velocity dispersion, are very similar for the different molecules and have values <20% of the gravitational energy. In addition, it was pointed out that these values likely are an upper limit. The relation for [C II], tracing the lower-density gas, is different, as it reaches up to 40%–60% of the gravitational energy. This seems to suggest that in the lower-density gas, which is particularly found at $r > 2$–3 pc, there might be significant thermal or turbulent support. However, it has to be taken into account that we found multiple velocity components that do not necessarily contribute to support against collapse in the region. The magnetic field energy depends on its assumed field strength evolution. Assuming $k = 0.5$ indicates that the cloud can experience some support from the magnetic field on large scales (∼3–4 pc), but gradually this magnetic support decreases, leading to an increasing importance of gravitational collapse when approaching the ridge ($r < 3$ pc). Assuming $k = 0.67$, the magnetic field provides little support at low densities, while the higher-density regions toward the ridge ($r < 1$ pc) experience an increased importance of the magnetic field. However, in both cases the values still indicate that the gravitational energy dominates over the cloud. This becomes particularly evident in Figure 14, where the total support terms over the gravitational terms are plotted. This shows that only considering $k = 0.5$ and the velocity dispersion of the [C II] emission allows for support against gravitational collapse, but this ignores that the [C II] velocity dispersion might not be associated with mass inflow rather than turbulent support.

5. Discussion

Combining the results and analysis from Sections 3 and 4, we will now discuss the cloud evolution leading to high-mass star formation in the DR21 ridge.

5.1. Magnetic Field Bending Followed by Gravitational Collapse in the DR21 Ridge

From the fitted velocity maps and PV diagrams we found indications of an accelerating velocity field, based on the rapid line width increase in the ridge and a blueshifted asymmetry in the self-absorbed molecular lines toward the ridge. Additionally, the observations showed that basically all subfilaments and the surrounding cloud appear to be organized in a flattened structure that gives rise to a redshifted V shape perpendicular to the ridge. [C II] also displays a second blueshifted velocity component that is localized in the vicinity of the ridge and looks like a more localized blueshifted V shape.

The accelerating velocity field can be the result of the proposed gravitationally driven inflow (e.g., Peretto et al. 2006; Hartmann & Burkert 2007). However, to explain the observed redshifted V-like velocity field in the surrounding cloud, as well as the systematic redshift of the subfilaments, we have to consider the apparent flattened geometry of the molecular cloud. If the flattened geometry is curved, this can provide a straightforward explanation for the observed velocity field if this curved sheet geometry is associated with the magnetic field bending in a collision as predicted by Hartmann et al. (2001), Inoue & Fukui (2013), Vaidya et al. (2013), Inoue et al. (2018), and Abe & Inoue (2021). The presence of a strong magnetic field in the compressed sheet might then even initially prevent gravitational acceleration and significantly affect the velocity field until the massive ridge is reached. We note that this is the same mechanism that was also proposed to explain the observations toward the Musca cloud, which has a very similar kinematic V shape perpendicular to the filament (Bonne et al. 2020b). There, it was proposed that Musca formed at the apex of a bent magnetic field as the result of an overdensity interacting with diffuse H I gas in a colliding flow. In fact, the DR21 region is proposed to be in a high-velocity ($v_{\rm col} \gtrsim$ 20 km s^{-1}) collision with the diffuse, mostly atomic regions of the other velocity component between $v_{\rm LSR} = 9$ and 15 km s^{-1} in the Cygnus X region (Schneider et al. 2023). This points to the same formation mechanism for the DR21 cloud as for the Musca cloud. However, the Cygnus X region is more than an order of magnitude more massive than the Chamaeleon−Musca region (e.g., Reipurth & Schneider 2008), and the

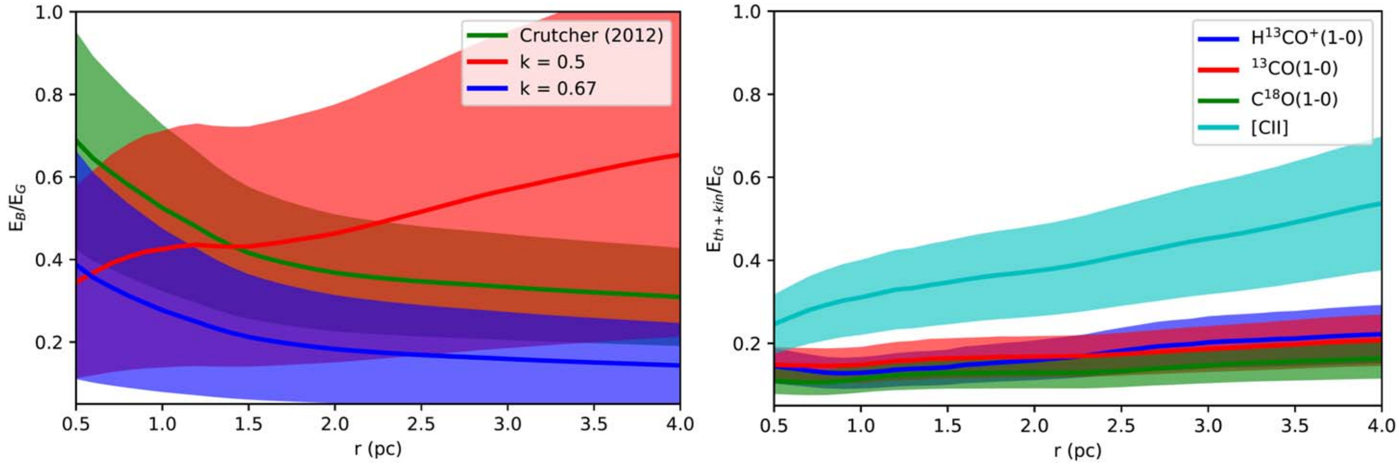

Figure 13. Ratio of the magnetic (left) and thermal + kinetic energy (right) over the gravitational energy as a function of the radius in the DR21 cloud. The radius is centered on DR21(OH). For the thermal + kinetic energy, the line widths of H^{13}CO$^+$ (1−0), ^{13}CO (1−0), C^{18}O (1−0), and [C II] are used. It appears that the regions of cloud traced by [C II] experience more support against gravitational collapse than the molecular regions. However, the presence of multiple components has to be kept in mind, which makes this an upper limit. The three approaches to estimate the magnetic field support are displayed on the left. It shows that the magnetic support is always smaller than the gravitational energy, but that the importance strongly depends on the assumptions for the magnetic field strength evolution.

collision velocity is higher, which can explain why the DR21 ridge is forming massive stars (e.g., Dobbs et al. 2020; Liow & Dobbs 2020). The second [C II] velocity component we found in the vicinity of the DR21 ridge at $v_{\rm LSR} \sim -4.5$ km s^{-1} is then likely gas associated with the $\gtrsim$20 km s^{-1} collision, responsible for the formation of the DR21 ridge, which leads to accretion on the ridge from the blueshifted side.

One could consider the scenario that the DR21 cloud is a swept-up shell created by expansion from a Local Bubble. However, there is no evident massive cluster candidate near the DR21 cloud that could drive the expansion of such a massive region (Maia et al. 2016), and the study of the multiple velocity components by Schneider et al. (2023) does not unveil a typical expanding shell morphology in the region.

In summary, we propose that the DR21 ridge was formed as the result of a high-velocity collision in the Cygnus X region, which bends the magnetic field around the ridge. This bending is at the origin of the inflow seen in the form of a kinematic V shape in the flattened surrounding cloud. However, due to the high density in the compressed cloud, gravity increasingly starts to dominate the curved kinematics driven by the magnetic field bending. This explains the observed accelerated motion in the ridge and the results from the virial analysis. The proposed scenario thus provides a comprehensive explanation for the rich set of observations that trace the density range of the DR21 cloud. Observations that trace the line-of-sight magnetic field morphology, and thus the proposed bending, would be invaluable to further test this scenario.

Lastly, we note that gravity did not take over the cloud kinematics in Musca (Bonne et al. 2020a). This is an important difference because the increasing importance of gravity on larger scales in the DR21 cloud allows more effective mass provision to the center(s) of collapse, e.g., the DR21(OH) and DR21-N clumps (Schneider et al. 2010).

5.2. *Mass Accretion on the DR21 Ridge*

The mass inflow toward the ridge guided by the subfilaments can be estimated using $\dot{M}_{\rm acc} = N\pi R^2 v_{\rm inf} n$ (Schneider et al. 2010; Peretto et al. 2013), with N the number of inflowing filaments, R the radius, n the density, and $v_{\rm inf}$ the velocity of the infalling filaments. Working with seven molecular inflowing subfilaments with $n = 10^5$ cm^{-3}, $R = 0.1$ pc (Hennemann et al. 2012), and an inflow velocity of 1–2 km s^{-1}, we get an estimated mass accretion rate of (1.3–2.6) × 10^{-3} $M_\odot$ yr^{-1}, similar to the estimate of Schneider et al. (2010). In Schneider et al. (2010), it was also shown that the F3 subfilament continues its flow toward the DR21(OH) clump in the ridge and may provide inflow to multiple massive dense cores. However, this mass inflow rate is roughly an order of magnitude lower than the required mass accretion rate ($\sim$10^{-2} $M_\odot$ yr^{-1}) to replenish the DR21 ridge within 1 Myr.

Taking into account that the mass inflow probably also happens off the subfilaments, we can calculate this contribution of mass inflow to the ridge. We consider inflow over the full surface of the ridge, for which we assume a cylindrical geometry with $R = 0.36$ pc and $L = 4.15$ pc (Hennemann et al. 2012). For the inflow, we work with a velocity of ∼1–2 km s^{-1} and $n = 10^4$ cm^{-3}, which is justified by $N_{\rm H_2} \sim 3 \times 10^{22}$ cm^{-2} within the 1 pc vicinity of the ridge. This density is at the high range of densities in the ambient gas, which can be expected if the gas is gravitationally concentrated when approaching the ridge. These values give an estimated mass accretion rate of (0.56–1.1) × 10^{-2} $M_\odot$ yr^{-1}, which can replenish the DR21 ridge in 1–2 Myr. Note that this might be an overestimate up to a factor ∼2, as the inflow is predominantly sideways in the sheet and not uniform. An expected lifetime for the DR21 ridge is 1–2 Myr when taking the expression from Clarke & Whitworth (2015) for the timescale of a free-fall longitudinal collapse for a filament:

$$\tau_{\rm ff} = (0.49 + 0.26\,A)(G\,\rho)^{-\frac{1}{2}}, \tag{8}$$

where A (=5.8) is the initial aspect ratio of the filament half-length over the filament radius and ρ (=3.9 × 10^{-19} g cm^{-3}) is the average density of the ridge. This results in a $\tau_{\rm ff}$ of 0.39 Myr. Considering support against longitudinal collapse from the magnetic field, which is perpendicular to the DR21 ridge at the center (Vallée & Fiege 2006; Matthews et al. 2009; Ching et al. 2022), 1−2 Myr likely is an appropriate timescale to replenish the DR21 ridge. We thus propose that the DR21

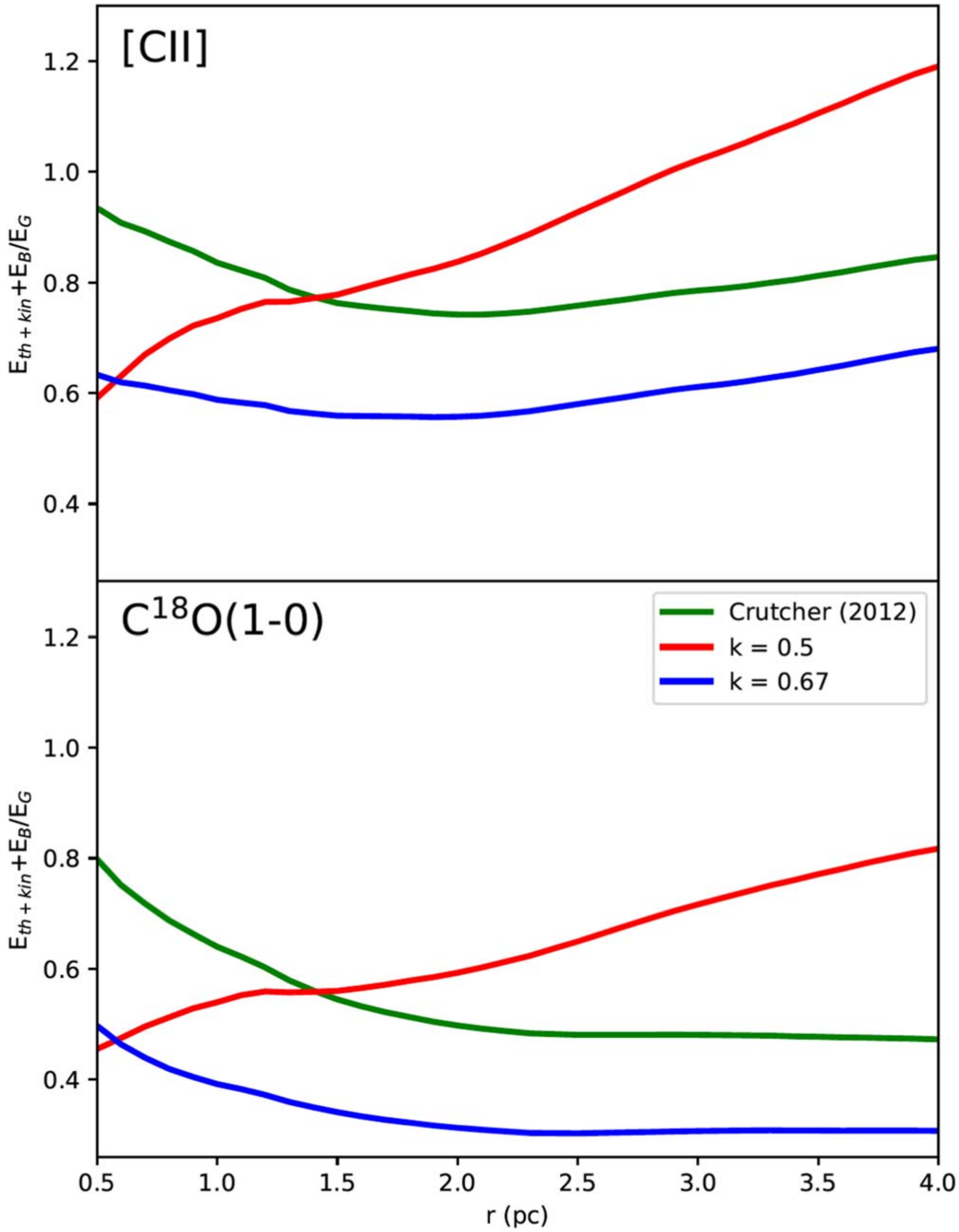

Figure 14. The ratio of the energy terms that provide support, i.e., $E_{\mathrm{th+kin}}$ and E_B, over the gravitational energy as a function of radius in the DR21 cloud. This is shown for [C II] (top), which has the largest line width, and C^{18}O (1−0) (bottom), which has the smallest line width. Only when considering [C II] and a $k = 0.5$ evolution of the magnetic field do the support terms get larger than the gravitational energy at $r > 3$ pc.

ridge can be continuously replenished by mass inflow from the surrounding cloud.

Only when feedback from the newly formed massive stars disperses the dense ridge and prevents further mass accretion will active high-mass star formation end. This dispersal of the ridge by stellar feedback, which is proposed to happen on relatively short timescales after the first massive stars form (i.e., $\lesssim$3 Myr; Hollyhead et al. 2015; Luisi et al. 2021; Bonne et al. 2022b; Chevance et al. 2022), might thus be important to maintain a low star formation efficiency. Even though stellar feedback might halt mass provision to the ridge, it is observed around the DR21 radio continuum source that regions of dense gas a bit farther out, in particular the nearby subfilaments (S and SW), remain present. This might be able to maintain continued lower-mass star formation while stellar feedback is already dispersing the ridge. For example, low-mass cores were detected in the subfilament F3 (Hennemann et al. 2012).

5.3. The Link with High-mass Star Formation

The above scenario implies that high-mass star formation might only occur over an interval of the total star formation time in a cloud. In the DR21 cloud, the formation of high-mass stars would be directly related to the lifetime of the massive ridge. This potentially shorter phase of high-mass star formation might fit with the observed shallow slope of the core mass function (CMF) in high-mass star-forming regions (Liu et al. 2018; Motte et al. 2018b; Pouteau et al. 2022) compared to the power-law tail of the initial mass function (IMF), as well as the slightly shallower IMFs in young clusters (< 4 Myr) of Cygnus X (Maia et al. 2016). However, further work with, e.g., the ALMA-IMF sample (Motte et al. 2022) will be needed to better understand the evolution of these top-heavy CMFs in high-mass star-forming regions and how it connects with the IMF of young stellar clusters, as well as the evolution of high-mass star-forming clouds and filaments (Pouteau et al. 2022).

6. Conclusion

We have presented new molecular line data of ^{13}CO (1−0), C^{18}O (1−0), HCO$^+$ (1−0), and H^{13}CO$^+$ (1−0) from the IRAM 30 m telescope and a [C II] map from the FEEDBACK SOFIA legacy survey of the DR21 cloud. In this study, we exclusively focus on the emission between −8 and 1 km s^{-1}, which is associated with the DR21 cloud, for all lines.

The molecular lines trace the dense ridge ($N_{\rm H_2}>10^{23}$ cm^{-2}) and subfilaments, while [C II] traces the surrounding molecular cloud (i.e., $N_{\rm H_2}\lesssim 10^{22}$ cm^{-2}) that embeds these filamentary structures. We demonstrate that this surrounding cloud seen with [C II] is mostly CO-poor. In both the molecular and [C II] spectra we find indications of more than one velocity component within the studied velocity range. We also note that there is an offset for the peak velocity in the cloud between the [C II] and molecular lines, confirming that they trace different regions of the cloud. Inside the ridge, the molecular lines confirm the results from Schneider et al. (2010), while the observations of the subfilaments show that they are systematically redshifted with respect to the ridge. The [C II] kinematics show a redshifted V-like shape, between −3 and −1 km s^{-1}, perpendicular to the ridge that intersects with a more blueshifted velocity component (at $v_{\rm LSR}\sim -5$ km s^{-1}) at the location of the ridge. We confirm that these two intersecting velocity components converge and that there is continuous mass accretion on the DR21 ridge. The V-shape velocity field embeds all the redshifted subfilaments, and density requirements to explain the observed [C II] emission indicate that the V shape has a flattened morphology. Tracing the CO-poor gas, seen in [C II] toward the DR21 cloud, is thus essential for a comprehensive view on cloud evolution and filament formation.

Performing a virial analysis, including estimates for the magnetic field support, we find that the cloud should be gravitationally collapsing on parsec scales. The surrounding gas traced by [C II] appears to have more support against gravitational collapse, but this does not take into account the organized velocity field and the presence of two velocity components that are not associated with turbulent support.

We propose that there is continuous mass accretion onto the DR21 ridge. This accretion is initiated by the bending of the magnetic field around the ridge due to a large-scale collision. In this collision, an overdensity is compressed into a dense filament/ridge during the interaction with diffuse atomic regions of the colliding cloud. However, because of the high density in the DR21 cloud, gravity is taking over the cloud dynamics, which facilitates rapid mass provision to a (few) center(s) of collapse where massive clusters are forming. We found that the continuous mass inflow, visible thanks to [C II], can replenish the ridge. Therefore, we propose that the DR21 ridge will remain present until stellar feedback disperses it and halts massive star formation.

Lastly, we note that this scenario is the same as proposed for the low-mass Musca cloud (Bonne et al. 2020a), except for the increasing importance of gravitational collapse in the massive DR21 cloud. This hints that the same scenario might be at the origin of filament formation in both a low- and high-mass star-forming region. Furthermore, recent magnetic field and velocity observations of some nearby low- and high-mass star-forming regions (e.g., Arzoumanian et al. 2022; Tahani 2022) appear to have a straightforward explanation in this scenario. This leads us to tentatively propose that these types of collisions are a widespread mechanism in the Milky Way to initiate a wide variety of star formation activity in the Milky Way.

Acknowledgments

We thank the anonymous referee for insightful comments that improved the content and clarity of the paper. We thank W. Lim and F. Comeron for insightful comments on an early draft of the paper. Based in part on observations made with the NASA/DLR Stratospheric Observatory for Infrared Astronomy (SOFIA). SOFIA is jointly operated by the Universities Space Research Association, Inc. (USRA), under NASA contract NAS2-97001, and the Deutsches SOFIA Institut (DSI) under DLR contract 50 OK 0901 to the University of Stuttgart.

This work was supported by the Agence National de Recherche (ANR/France) and the Deutsche Forschungsgemeinschaft (DFG/Germany) through the project "GENESIS" (ANR-16-CE92-0035-01/DFG1591/2-1) and the DFG project No. SFB 956. The FEEDBACK project is supported by the Federal Ministry of Economics and Energy (BMWI) via DLR, Projekt No. 50 OR 2217 (FEEDBACK-plus). Financial support for the SOFIA Legacy Program, FEEDBACK, at the University of Maryland was provided by NASA through award SOFO070077 issued by USRA.

Facilities: SOFIA (upGREAT), IRAM 30m, Herschel, JCMT.

Software: astropy (Astropy Collaboration et al. 2013).

Appendix A
[C II] and James Clerk Maxwell Telescope ^{12}CO (3–2) Observations

In Figure 15 we present a comparison of the [C II] integrated intensity and JCMT ^{12}CO (3–2) integrated intensity. These JCMT data over the full Cygnus X region will be the topic of a forthcoming paper. Because of the larger column density than for ^{13}CO, the ^{12}CO emission is detected further into the cloud compared to ^{13}CO (see Figure 2). However, ^{12}CO still is particularly sensitive to the massive ridge and surrounding subfilaments and has a clearly distinct morphology compared to [C II]. This confirms that [C II] provides a unique view on the lower column density gas that is not accessible with molecular lines.

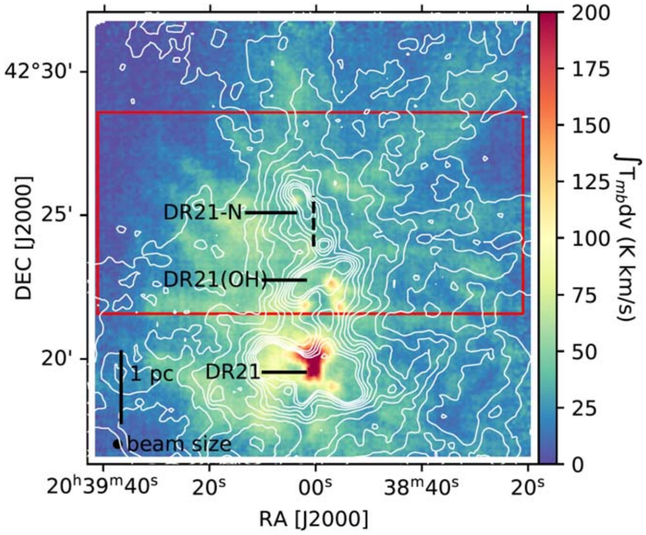

Figure 15. The [C II] integrated intensity map from −8 to 1 km s^{-1} as in Figure 3. Here the contours indicate the JCMT ^{12}CO (3–2) emission starting at 20 K km s^{-1} with incremental steps of 20 K km s^{-1}.

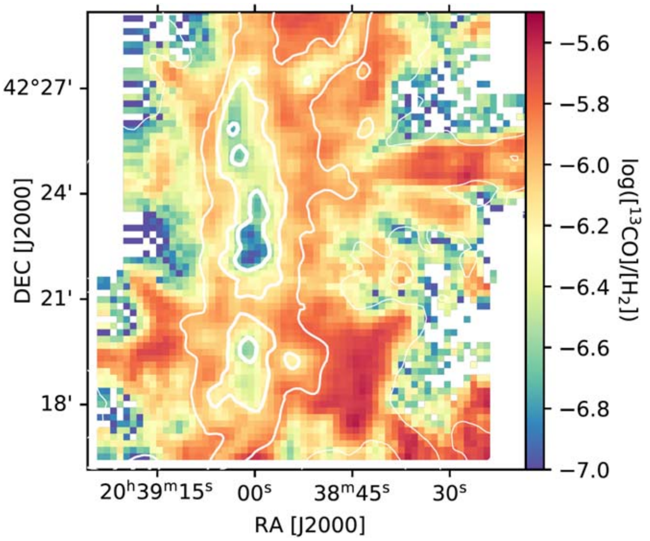

Figure 16. Map of the ^{13}CO abundance on a log scale over the DR21 cloud. This is deduced from the ^{13}CO (1−0) intensity, a kinetic temperature of 18 K, and the Herschel column density map. The white contours indicate the Herschel column density map at $N = 10^{22}$ cm^{-2}, 3×10^{22} cm^{-2}, 10^{23} cm^{-2}, and 4×10^{23} cm^{-2}.

Appendix B
The ^{13}CO Abundance

The calculation of the ^{13}CO column density map allows us to estimate ^{13}CO abundance based on the background-subtracted Herschel column density map (Schneider et al. 2016a). This then allows us to explore which regions of the cloud are traced by the observed ^{13}CO (1−0) transition. The calculation of the ^{13}CO column density follows the calculations presented in Mangum & Shirley (2015). Below we recapitulate the equations and values used. Note that these equations assume that the molecule is optically thin. This assumption is not necessarily valid for ^{13}CO (1−0) over the full map, in particular at the ridge. However, due to the high density in the ridge, which will result in freeze-out of the molecule, the opacity should not be excessive even in these regions of very high column density. When studying the outer regions of the ridge and the ambient gas, C^{18}O is barely detected, which implies that the ^{13}CO opacity will not be significantly above 1 for standard isotopologue ratios. Nonetheless, it has to be kept in mind that this assumption is a limitation of the calculations below.

The total column density is then calculated from

$$N\,[\mathrm{cm}^{-2}] = f\,(T_{\mathrm{ex}}) \int T_{\mathrm{mb}}\,dv. \tag{9}$$

Here T_{mb} is the main-beam brightness in kelvin, v is the velocity in kilometers per second, and $f(T_{\mathrm{ex}})$ is given by

$$f\,(T_{\mathrm{ex}}) = \frac{3hZ}{8\pi^3\mu^2 J_t}\frac{\exp(h\nu/kT_{\mathrm{ex}})}{[1-\exp(-h\nu/kT_{\mathrm{ex}})](J\,(T_{\mathrm{ex}})-J\,(T_{\mathrm{BG}}))}. \tag{10}$$

In this equation, Z is the partition function,

$$Z = \frac{2kT_{\mathrm{ex}}}{h\nu} + 1/3, \tag{11}$$

with k the Boltzmann constant, h the Planck constant, ν the transition frequency (for ^{13}CO (1−0) this is 110.201 GHz), and T_{ex} the excitation temperature (for which we assume a value of 18 K; see also Schneider et al. 2010).

Further in the equation of $f(T_{\mathrm{ex}})$, μ is the dipole moment (for ^{13}CO (1−0) this is 0.112 D), J_t is the upper value of the rotational quantum number (i.e., 1), and $J(T_{\mathrm{ex}})$ is given by

$$J\,(T_{\mathrm{ex}}) = \frac{h\nu}{k\,[\exp(h\nu/kT_{\mathrm{ex}})-1]}. \tag{12}$$

For the background, a temperature of 2.73 K is assumed based on the cosmic microwave background.

The estimated ^{13}CO abundance map, based on the Herschel column density map, is presented in Figure 16. Using the assumptions above, ^{13}CO is most abundant at the edges of the ridge and in the subfilaments (F3N, F3S, and SW in particular). Inside the ridge, there is a significant decrease with increasing column density (see also Figure 17), which is expected because of CO depletion at densities $n_{\mathrm{H_2}} > 10^4$ cm^{-3}. To trace the DR21 ridge kinematics, one thus needs to rely on tracers like HCO$^+$, N$_2$H$^+$, and deuterated molecules to probe the very dense gas of the ridge. In the surrounding cloud, at $N_{\mathrm{H_2}} < 1.5 \times 10^{22}$ cm^{-2}, where ^{13}CO is detected, there is also an observed lower ^{13}CO abundance. Indeed, Figure 17 shows that the ^{13}CO abundance starts decreasing again toward lower column densities. This is the result of an increasing CO-dark gas fraction in the DR21 cloud below these column densities. From Figure 17, it is also observed that at $N_{\mathrm{H_2}} < 1.5 \times 10^{22}$ cm^{-2} the [C II] abundance continues to increase up to the typical carbon abundance in the ISM. This indicates that [C II] allows us to trace the CO-dark gas in the surrounding DR21 cloud.

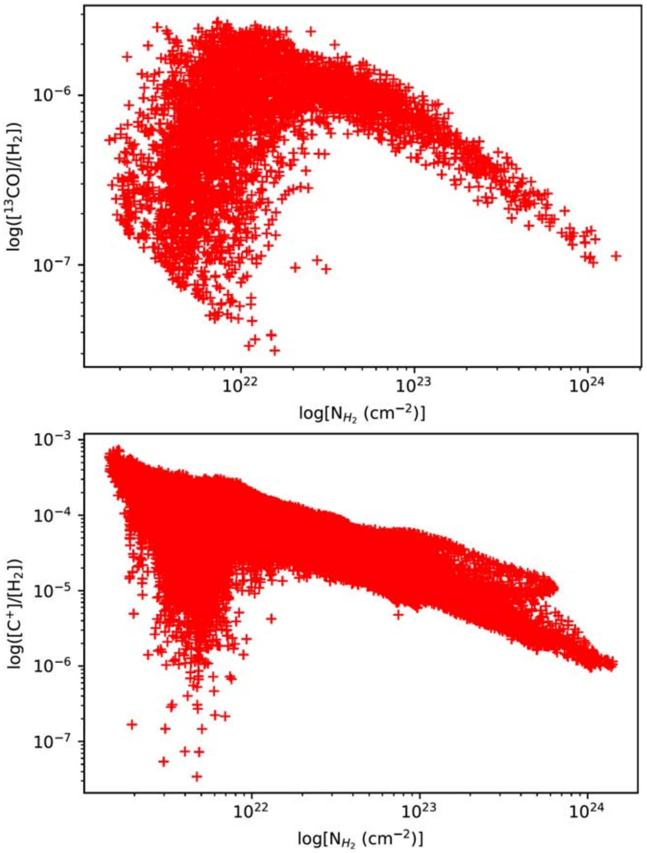

Figure 17. Top: ^{13}CO abundance as a function of the Herschel column density for all pixels in the map. Bottom: same as the top panel, but for the C$^+$ abundance.

Table 2
Results Produced with RADEX for Conditions (N(C$^+$), $n_{\mathrm{H_2}}$, T_{kin}, FWHM) That Could Be Representative of the [C II]-emitting Gas

N(C$^+$) (10^{17} cm^{-2})	T_{kin} (K)	$n_{\mathrm{H_2}}$ (cm^{-3})	FWHM (km s^{-1})	τ	T_R (K)
5.0	30	10^4	4.0	7.7×10^{-1}	1.6
5.0	50	10^4	4.0	6.1×10^{-1}	5.2
5.0	75	10^4	4.0	4.7×10^{-1}	9.0
5.0	100	10^4	4.0	3.9×10^{-1}	1.2×10^1
8.0	30	10^4	4.0	1.2	2.2
8.0	50	10^4	4.0	9.7×10^{-1}	7.4
5.0	30	10^3	4.0	8.2×10^{-1}	4.3×10^{-1}

Note. T_R is the radiation temperature, which is equivalent to the main-beam temperature under the assumption that the beam filling is unity (this should be a reasonable assumption seeing the extended [C II] emission). The optical depth (τ) predictions are basically always below unity, which suggests relatively optically thin [C II] emission.

Appendix C
The [C II] Optical Depth

In order to constrain the [C II] optical depth toward the DR21 cloud, and in particular the ridge, we work with the average spectrum over the ridge in order to reduce the noise rms. This decrease in noise rms is important in order to try to detect the [^{13}C II] hyperfine structure lines that are located at −65.2 km s^{-1} (F = 1–0), 11.7 km s^{-1} (F = 2−1), and 62.4 km s^{-1} (F = 1–1) with respect to the [C II] line. The hyperfine structure lines have a relative strength of 0.25 (F = 1–0), 0.625 (F = 2 −1), and 0.125 (F = 1–1). Ideally, one thus works with the $F = 2-1$ transition, but this line is very close to the actual [C II] emission and contaminated by the observed bridging with a higher-velocity component (Schneider et al. 2023). At the location of the $F = 2-1$ transition no indication of additional [^{13}C II] emission is found (see Figure 18), but we will not work with this transition because of the confusion from the actual [C II] emission. Therefore, we focus on the second-brightest transition (F = 1–0) at −65.2 km s^{-1}. Figure 18 shows that this transition is not detected at a noise rms of 7.6×10^{-1} K within 0.5 km s^{-1} for the averaged spectrum. Although not detected, we still try to obtain an idea of the optical depth associated with this noise level. This can be done using the equation

$$\frac{T_{\mathrm{mb},12}}{T_{\mathrm{mb},13}} = \frac{1 - e^{-\tau}}{\tau}\alpha, \tag{13}$$

with τ the optical depth and α the local ^{12}C/^{13}C abundance, for which we take a value of 60 (Wilson & Rood 1994) and a correction factor of 0.25 for the relative strength of the F = 1–0 transition. Then, using the noise rms value (7.6×10^{-1} K) results in an optical depth of $\tau = 1.7$. Since the F = 1–0 transition is not detected, this indicates that $\tau = 1.7$ rather is an upper limit, which indicates that the [C II] line is optically thin or marginally optically thick at best toward the DR21 ridge.

To further investigate the potential optical depth of the [C II] line, we also run RADEX simulations (van der Tak et al. 2007) using input values obtained in this paper for the [C II]-emitting region toward the DR21 ridge. These calculations are presented in Table 2, which shows that the predicted optical depth typically is below unity. Note that the highest obtained optical depths, which are still only of the order of unity and occur at

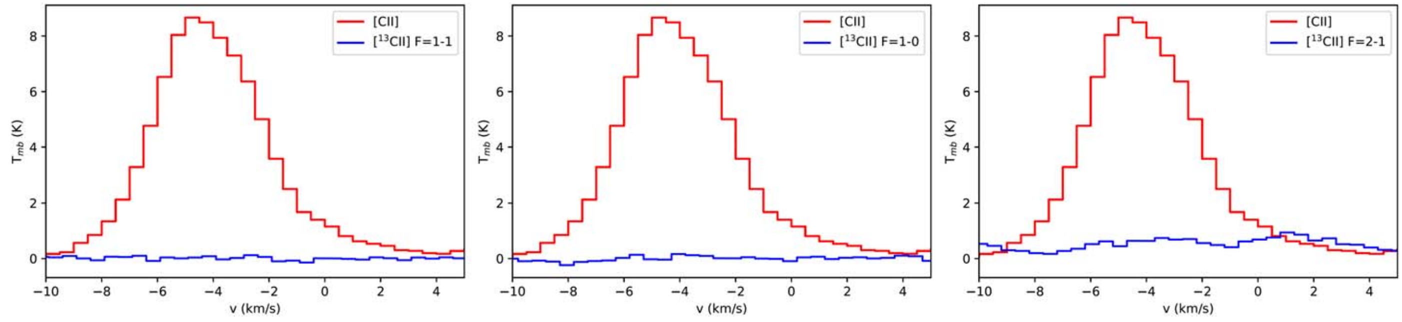

Figure 18. Left: [^{13}C II] F = 1–0 transition shifted to the same velocity as the [C II] line. There is no detected counterpart for this [^{13}C II] transition at the velocities of the DR21 ridge component. Middle: same as the left panel, but for the [^{13}C II] F = 1–1 transition. Right: same as the left panel, but for the [^{13}C II] F = 2−1 transition. For this transition, there is confusion from the higher-velocity components (Schneider et al. 2023). Therefore, we do not use this transition here.

$T_{\rm kin} \approx 30$ K, have a too low corresponding line brightness such that they likely are not representative for the observed emission. This is in agreement with the results from Section 4.1, which indicates that the kinetic temperature in the [C II]-emitting gas is likely of the order of 100 K (for which we obtain lower optical depths).

Appendix D
[C II] Multicomponent Fit

As the [C II] emission likely is not optically thick, we examine here whether more than one Gaussian component is required to explain the observed [C II] line spectral-line profiles. To fit all spectra over the full map within the −8 to 1 km s^{-1} velocity range, we employ the BTS fitting tool, which is updated with the Akaike information criterion (AIC; Clarke et al. 2018, 2019, in preparation). However, we do exclude the DR21 radio continuum source and associated outflow from the analysis. As the [C II] noise rms is still relatively high at the native resolution, which can mask multiple velocity components, we smoothed the data to a spatial resolution of 30″. This value was taken to balance significantly reducing the noise rms while avoiding the inclusion of large velocity gradients in a single beam, which would give rise to additional velocity components. Note that the 30″ data are also used in Schneider et al. (2023). In the fitting iteration procedure, when a fit has been done with n velocity peaks, the fit will be repeated with $n-1$ and $n+1$ velocity peaks and the corrected AIC is calculated for each new fit. Then, the fit with the smallest number of velocity peaks is chosen unless a higher number of velocity peaks is smaller by $\Delta_{\rm AIC} > 10$ (see, e.g., Clarke et al. 2019 for the equations). This process is iterated until the number of peaks does not change anymore. The defined $\Delta_{\rm AIC}$ parameter was found to be robust not to overfit noisy spectra, in particular for large spectral cubes (S. D. Clarke et al. 2023, in preparation).

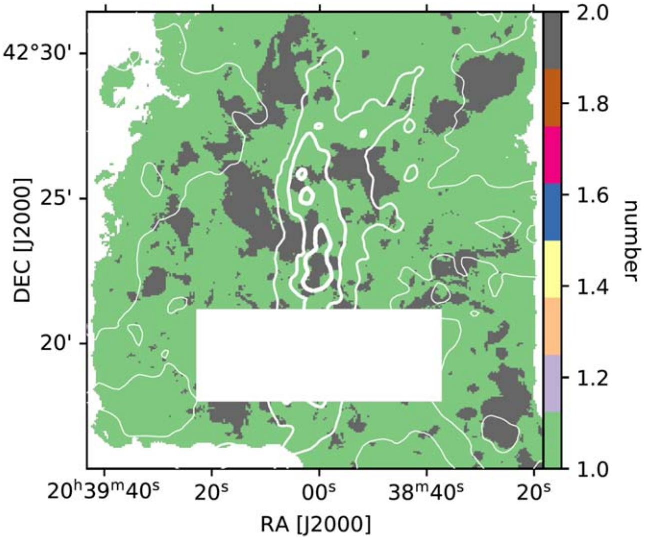

Figure 19. Number of fitted velocity components within the −8 to 1 km s^{-1} velocity range. The white box indicates the region around the DR21 radio continuum source and its associated outflow, which artificially increases the number of fitted velocity components. The white contours indicate the Herschel column density at $N_{\rm H_2} = 10^{22}$ cm^{-2}, 3×10^{22} cm^{-2}, 10^{23} cm^{-2}, and 4×10^{23} cm^{-2}.

The resulting number of velocity components over the map in the −8 to 1 km s^{-1} velocity range is presented in Figure 19. This demonstrates that the regions with two velocity components are in particular located at the edge of the DR21 ridge. To test this result, we also fitted the [C II] data cube between −8 and 1 km s^{-1} at the 20″ resolution. This demonstrated a similar spatial distribution of the two velocity components, the only difference being that the procedure found fewer pixels with two velocity components because of the higher noise rms at this resolution. Comparing the number of velocity components with the [C II] velocity field in Figure 20, we find that regions

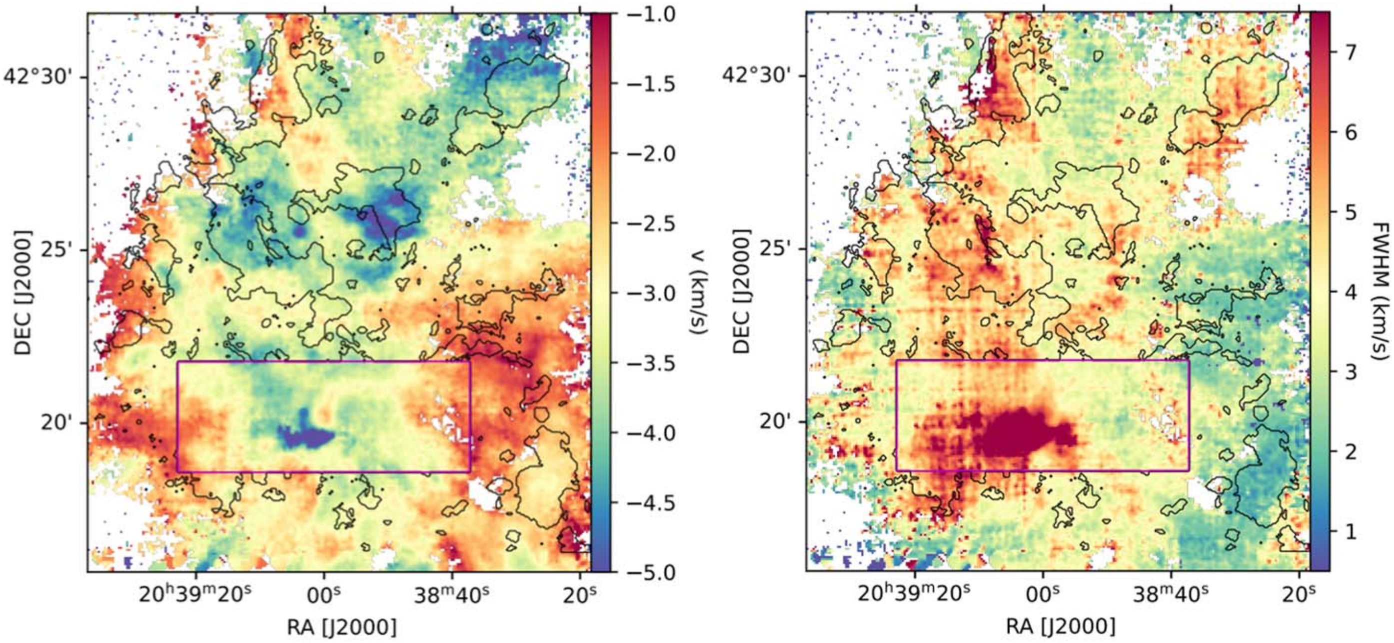

Figure 20. Left: [C II] velocity field from Figure 7, with the black contours indicating the regions that are fitted with two velocity components between $v_{\rm LSR}$ −8 and 1 km s^{-1}. Right: same as the left panel, but for the [C II] FWHM map.

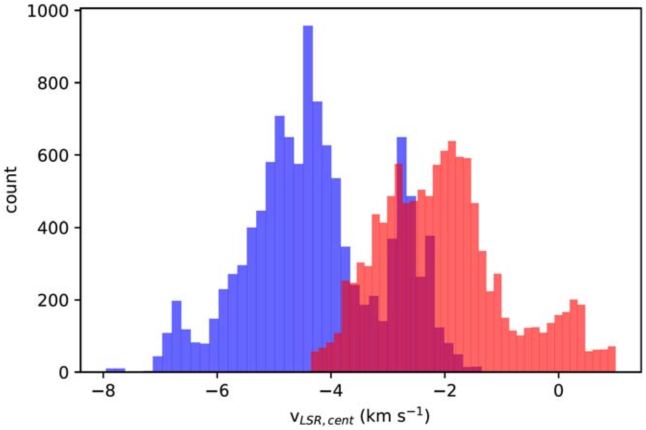

Figure 21. Peak velocity distribution of the blueshifted (blue) and redshifted (red) velocity components of the double-Gaussian fit to the data.

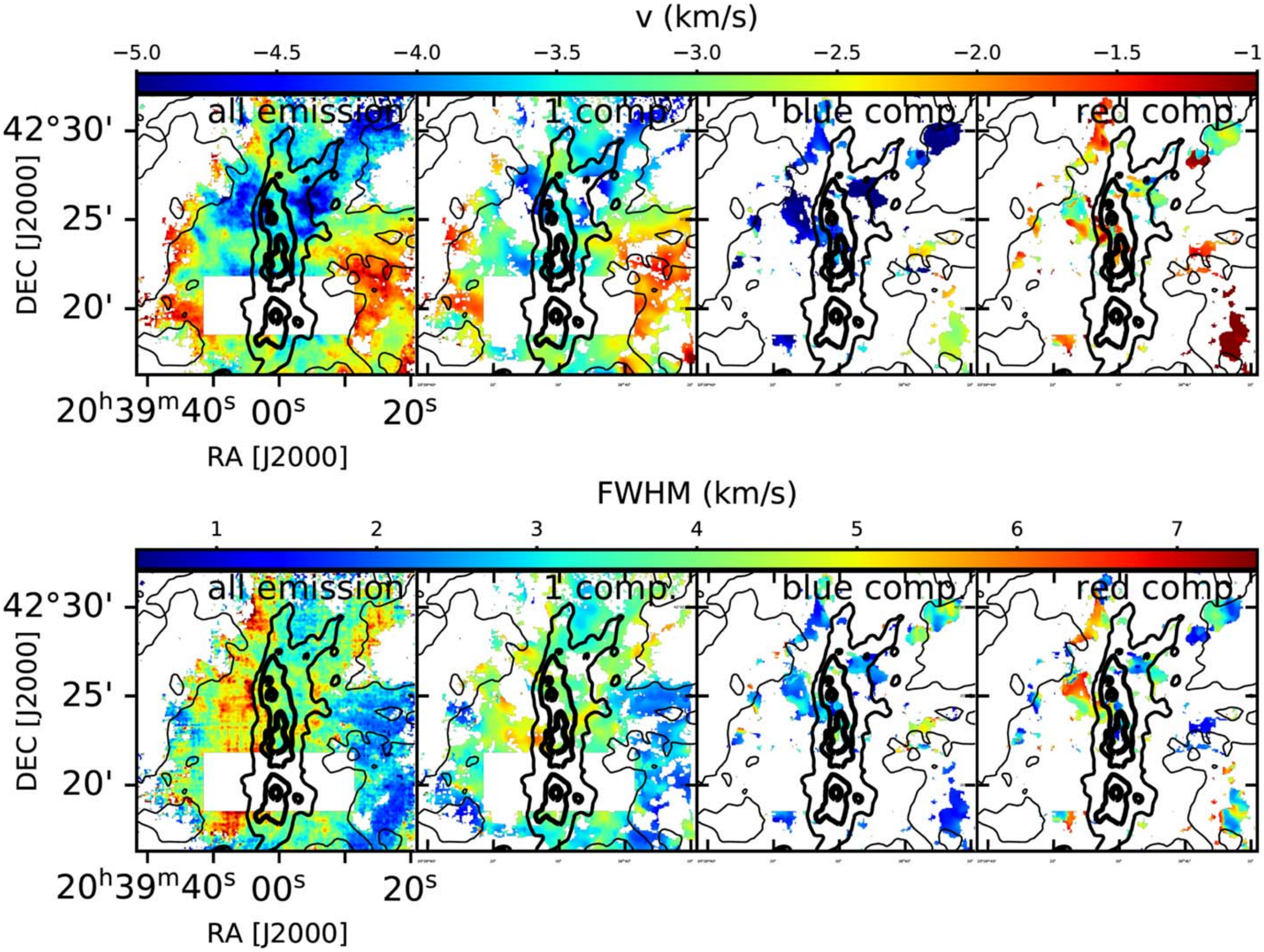

Figure 22. Top left: the [C II] velocity field of the DR21 cloud when taking into account all emission between −8 and 1 km s^{-1}. The black contours indicate the Herschel column density at $N_{\mathrm{H}_2} = 10^{22}$ cm^{-2}, 3 × 10^{22} cm^{-2}, 10^{23} cm^{-2}, and 4 × 10^{23} cm^{-2}. Middle left: the [C II] velocity field in the pixels that have only one velocity component. Middle right: the [C II] velocity field of the blueshifted component in the pixels that were fitted with two Gaussian components. Right: the [C II] velocity field of the redshifted component in the pixels that were fitted with two Gaussian components. Bottom: same as the top panels, but for the FWHM.

with two velocity components have a close spatial correlation with the regions that have a blueshifted velocity in [C II]. This confirms that the location of the DR21 ridge is associated with the intersection of the proposed V-shape accretion flow with an additional velocity component. Lastly, Figure 21 shows the velocity distribution of the two fitted velocity components, while Figure 22 shows the associated maps for the velocity and line width. The more blueshifted velocity component is typically found within the range of -6 km s^{-1} and -4 km s^{-1}, while the redshifted component varies between -4 and -1 km s^{-1}. The typical velocity difference of the two converging components is between 2 and 3 km s^{-1}.

Appendix E
$C^{18}O$ (1–0) and $H^{13}CO^+$ (1–0) Multicomponent Fit

We also performed a multicomponent fit with the BTS fitting tool to the $C^{18}O$ (1–0) and $H^{13}CO^+$ (1–0) molecular lines between -8 and 1 km s^{-1}, as they are not affected by strong opacity or self-absorption effects. This shows that there are significant regions that host two resolved velocity components in both lines; see Figures 23 and 24. These regions are particularly in and at the edge of the DR21 ridge. It is noteworthy when inspecting these figures that the regions where the subfilaments connect to the ridge, which is associated with a high line width (FWHM $>$ 3 km s^{-1}), are fitted with a single velocity component. This suggests either that several velocity components blend closely together there or that there might be a rapid reorientation in the line-of-sight velocity of the inflow or accretion shocks. From the velocity field maps, it can be observed that these regions are associated with a significant change in velocity; see Figures 25 and 26. Inspecting the velocity distribution for the regions with two fitted components (see Figures 27 and 28), it is found that the interval for the redshifted velocity component is very similar for [C II] and the molecular lines. This tends to confirm that the redshifted filaments are embedded in the redshifted inflowing mass reservoir. However, for the blueshifted velocity components, it appears that [C II] emission is shifted toward more blueshifted velocities with respect to the emission in the molecular lines. This shift for the blueshifted [C II] velocity component fits with the fact that there are no blueshifted subfilaments and thus that the blueshifted envelope of the DR21 ridge has a different morphology than the redshifted envelope.

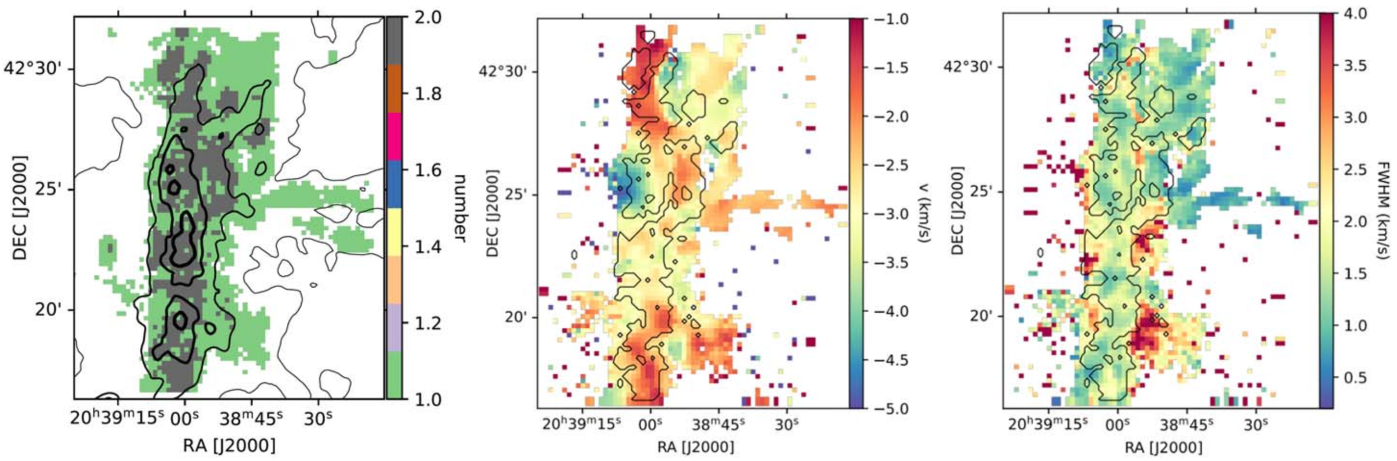

Figure 23. Left: same as Figure 19, but for $C^{18}O$ (1–0), with the column density contours in black. Middle and right: same as Figure 20, but for $C^{18}O$ (1–0).

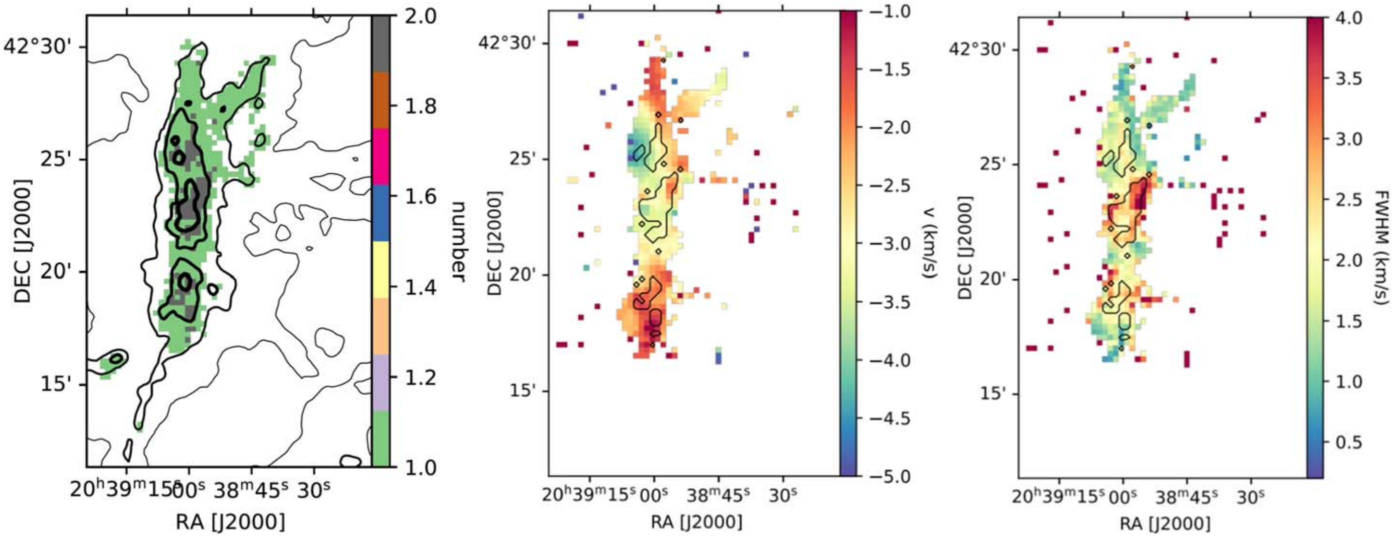

Figure 24. Same as Figure 23, but for $H^{13}CO^+$ (1–0).

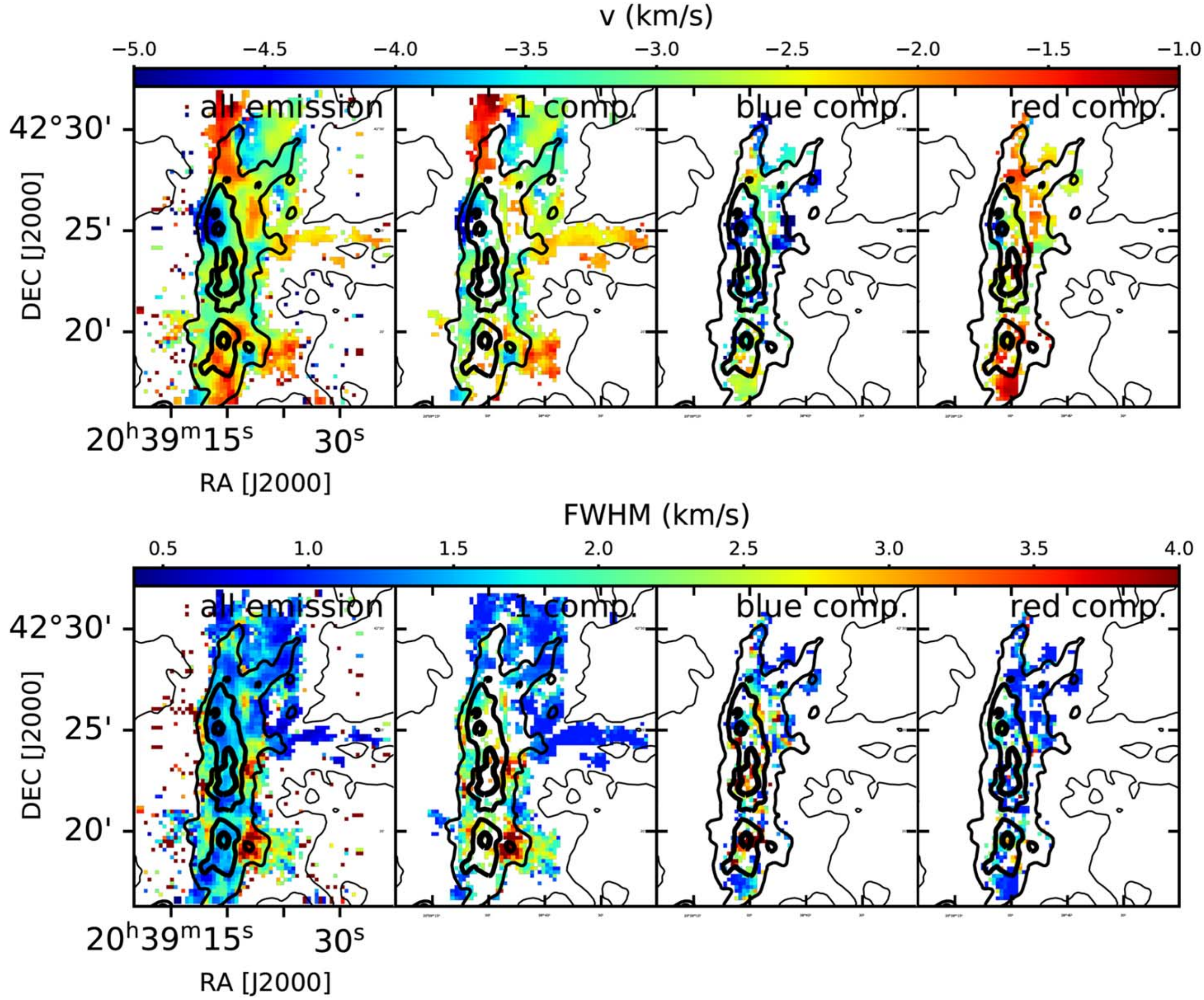

Figure 25. Same as Figure 22, but for $C^{18}O$ (1−0).

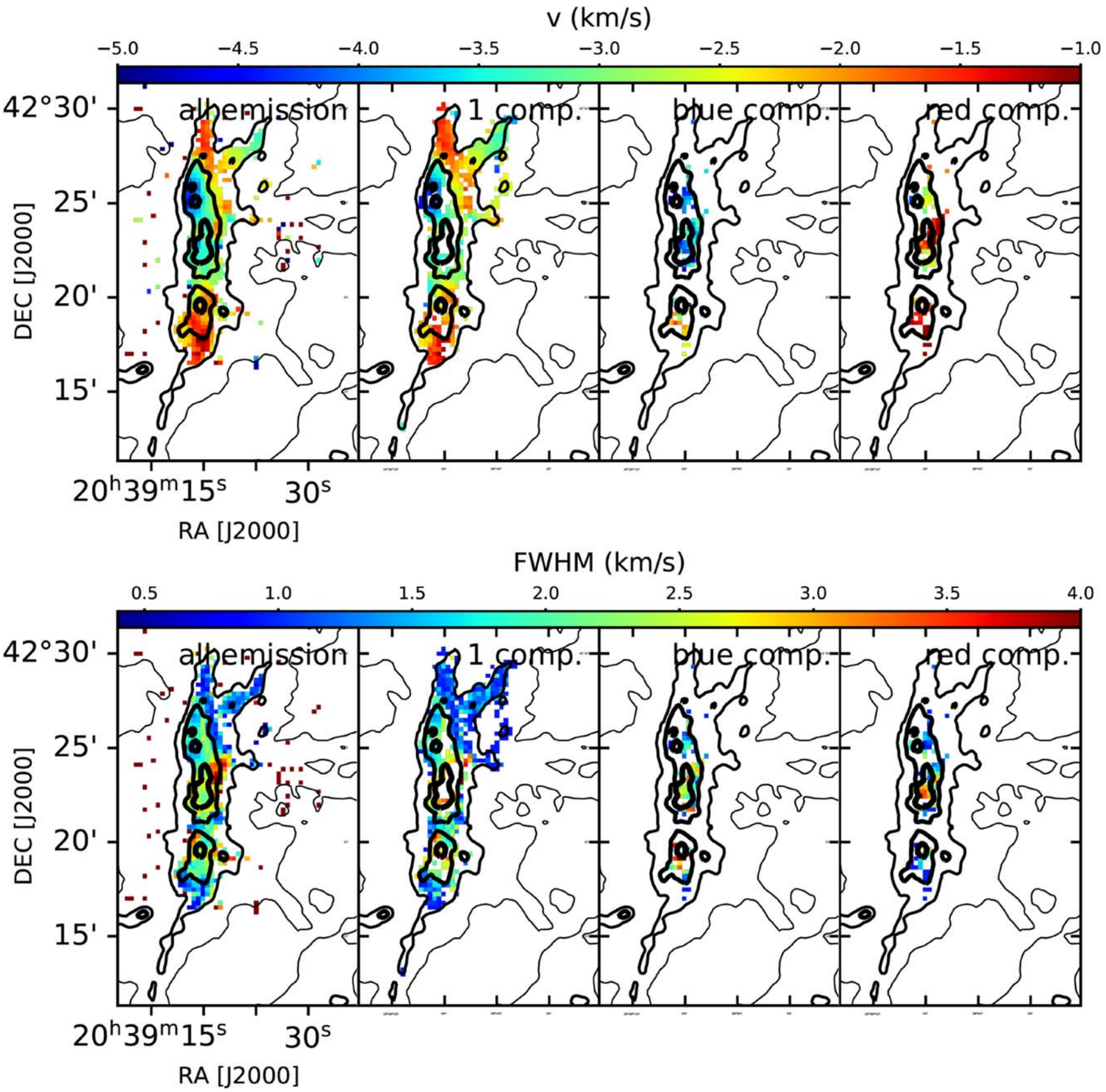

Figure 26. Same as Figure 22, but for $H^{13}CO^+$ (1−0).

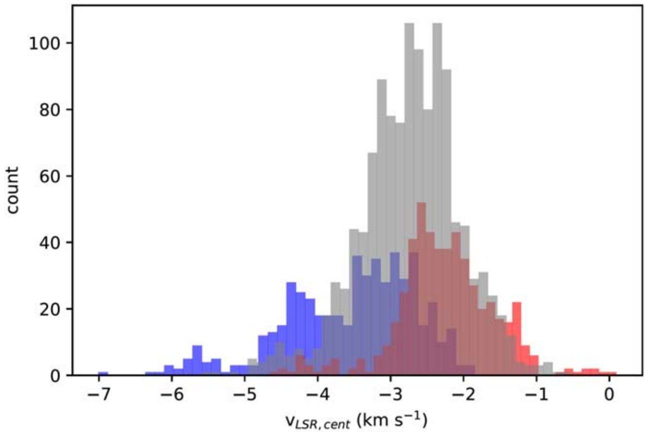

Figure 27. Same as Figure 21, but for $C^{18}O$ (1−0). The gray histogram indicates the peak velocity distribution for the pixels with a single fitted velocity component.

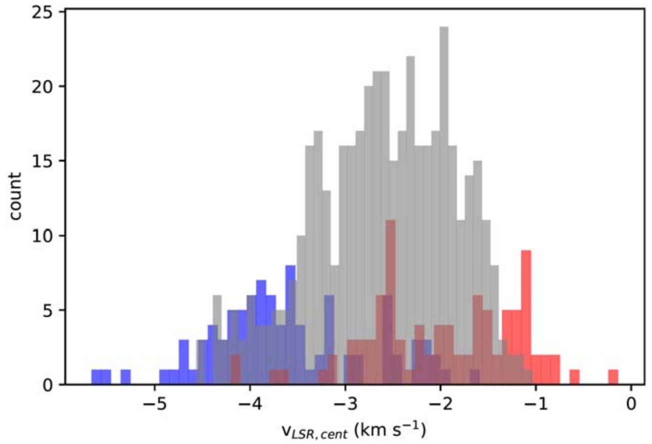

Figure 28. Same as Figure 27, but for $H^{13}CO^+$ (1−0).

ORCID iDs

L. Bonne https://orcid.org/0000-0002-0915-4853
N. Schneider https://orcid.org/0000-0003-3485-6678
R. Simon https://orcid.org/0000-0003-2555-4408
S. D. Clarke https://orcid.org/0000-0001-9751-4603
T. Csengeri https://orcid.org/0000-0002-6018-1371
E. Chambers https://orcid.org/0000-0003-4195-1032
U. Graf https://orcid.org/0000-0003-4439-6716
J. M. Jackson https://orcid.org/0000-0002-3466-6164
R. Klein https://orcid.org/0000-0002-7187-9126
Y. Okada https://orcid.org/0000-0002-6838-6435
A. G. G. M. Tielens https://orcid.org/0000-0003-0306-0028
M. Tiwari https://orcid.org/0000-0003-4260-2950

References

Abe, D., Inoue, T., Inutsuka, S., & Matsumoto, T. 2021, ApJ, 916, 83
Arzoumanian, D., Russeil, D., Zavagno, A., et al. 2022, A&A, 660, A56
Astropy Collaboration, Robitaille, T. P., Tollerud, E. J., et al. 2013, A&A, 558, A33
Balfour, S. K., Whitworth, A. P., & Hubber, D. A. 2017, MNRAS, 465, 3483
Basu, S. 1997, ApJ, 485, 240
Beerer, I. M., Koenig, X. P., Hora, J. L., et al. 2010, ApJ, 720, 679
Bertoldi, F., & McKee, C. F. 1992, ApJ, 395, 140
Beuther, H., Henning, T., Linz, H., et al. 2015, A&A, 581, A119
Bisbas, T. G., Tan, J. C., Csengeri, T., et al. 2018, MNRAS, 478, L54
Bisbas, T. G., Tanaka, K. E. I., Tan, J. C., Wu, B., & Nakamura, F. 2017, ApJ, 850, 23
Bonne, L., Bontemps, S., Schneider, N., et al. 2020a, A&A, 644, A27
Bonne, L., Peretto, N., Duarte-Cabral, A., et al. 2022a, A&A, 665, A22
Bonne, L., Schneider, N., Bontemps, S., et al. 2020b, A&A, 641, A17
Bonne, L., Schneider, N., García, P., et al. 2022b, ApJ, 935, 171
Bonnell, I. A., & Bate, M. R. 2006, MNRAS, 370, 488
Bonnell, I. A., Bate, M. R., Clarke, C. J., & Pringle, J. E. 2001, MNRAS, 323, 785
Bonnell, I. A., Vine, S. G., & Bate, M. R. 2004, MNRAS, 349, 735
Bontemps, S., Motte, F., Csengeri, T., & Schneider, N. 2010, A&A, 524, A18
Bracco, A., Jelić, V., Marchal, A., et al. 2020, A&A, 644, L3
Chevance, M., Kruijssen, J. M. D., Krumholz, M. R., et al. 2022, MNRAS, 509, 272
Ching, T.-C., Lai, S.-P., Zhang, Q., et al. 2017, ApJ, 838, 121
Ching, T.-C., Qiu, K., Li, D., et al. 2022, ApJ, 941, 122
Clarke, S. D., & Whitworth, A. P. 2015, MNRAS, 449, 1819
Clarke, S. D., Whitworth, A. P., Spowage, R. L., et al. 2018, MNRAS, 479, 1722
Clarke, S. D., Williams, G. M., Ibáñez-Mejía, J. C., & Walch, S. 2019, MNRAS, 484, 4024
Crutcher, R. M., Wandelt, B., Heiles, C., Falgarone, E., & Troland, T. H. 2010, ApJ, 725, 466
Csengeri, T., Bontemps, S., Schneider, N., Motte, F., & Dib, S. 2011a, A&A, 527, A135
Csengeri, T., Bontemps, S., Schneider, N., et al. 2011b, ApJL, 740, L5
Csengeri, T., Urquhart, J. S., Schuller, F., et al. 2014, A&A, 565, A75
Cyganowski, C. J., Reid, M. J., Fish, V. L., & Ho, P. T. P. 2003, ApJ, 596, 344
Dickel, J. R., Dickel, H. R., & Wilson, W. J. 1978, ApJ, 223, 840
Dobashi, K., Shimoikura, T., Katakura, S., Nakamura, F., & Shimajiri, Y. 2019, PASJ, 71, S12
Dobbs, C. L., Liow, K. Y., & Rieder, S. 2020, MNRAS, 496, L1
Dobbs, C. L., Pringle, J. E., & Burkert, A. 2012, MNRAS, 425, 2157
Downes, D., & Rinehart, R. 1966, ApJ, 144, 937
Duarte-Cabral, A., Bontemps, S., Motte, F., et al. 2013, A&A, 558, A125
Duarte-Cabral, A., Bontemps, S., Motte, F., et al. 2014, A&A, 570, A1
Fukui, Y., Habe, A., Inoue, T., Enokiya, R., & Tachihara, K. 2021, PASJ, 73, S1
Galván-Madrid, R., Zhang, Q., Keto, E., et al. 2010, ApJ, 725, 17
Girichidis, P., Federrath, C., Banerjee, R., & Klessen, R. S. 2012, MNRAS, 420, 613
Glover, S. C. O., & Clark, P. C. 2012, MNRAS, 421, 9
Goldsmith, P. F., Langer, W. D., Pineda, J. L., & Velusamy, T. 2012, ApJS, 203, 13
Gómez, G. C., & Vázquez-Semadeni, E. 2014, ApJ, 791, 124
Gottschalk, M., Kothes, R., & Matthews, H. E. 2012, A&A, 541, A79
Graf, U. U., Simon, R., Stutzki, J., et al. 2012, A&A, 542, L16
Guan, X., Stutzki, J., Graf, U. U., et al. 2012, A&A, 542, L4
Guevara, C., Stutzki, J., Ossenkopf-Okada, V., et al. 2020, A&A, 636, A16
Hacar, A., Kainulainen, J., Tafalla, M., Beuther, H., & Alves, J. 2016, A&A, 587, A97
Hartmann, L., Ballesteros-Paredes, J., & Bergin, E. A. 2001, ApJ, 562, 852
Hartmann, L., & Burkert, A. 2007, ApJ, 654, 988
Haworth, T. J., Tasker, E. J., Fukui, Y., et al. 2015, MNRAS, 450, 10
Hennebelle, P., Commerçon, B., Joos, M., et al. 2011, A&A, 528, A72
Hennemann, M., Motte, F., Schneider, N., et al. 2012, A&A, 543, L3
Hill, T., Motte, F., Didelon, P., et al. 2011, A&A, 533, A94
Hill, T., Motte, F., Didelon, P., et al. 2012, A&A, 542, A114
Hollenbach, D. J., & Tielens, A. G. G. M. 1999, RvMP, 71, 173
Hollyhead, K., Bastian, N., Adamo, A., et al. 2015, MNRAS, 449, 1106
Hora, J. L., Bontemps, S., Megeath, S. T., et al. 2009, AAS Meeting Abstracts, 213, 356.01
Immer, K., Cyganowski, C., Reid, M. J., & Menten, K. M. 2014, A&A, 563, A39
Inoue, T., & Fukui, Y. 2013, ApJL, 774, L31
Inoue, T., Hennebelle, P., Fukui, Y., et al. 2018, PASJ, 70, S53
Jackson, J. M., Whitaker, J. S., Rathborne, J. M., et al. 2019, ApJ, 870, 5
Kabanovic, S., Schneider, N., Ossenkopf-Okada, V., et al. 2022, A&A, 659, A36
Kaufman, M. J., Wolfire, M. G., & Hollenbach, D. J. 2006, ApJ, 644, 283
Keown, J., Di Francesco, J., Rosolowsky, E., et al. 2019, ApJ, 884, 4
Klessen, R. S., & Hennebelle, P. 2010, A&A, 520, A17
Kramer, C., Penalver, J., & Greve, A. 2013, Improvement of the IRAM 30m telescope beam pattern, IRAM, https://publicwiki.iram.es/CalibrationPapers?action=AttachFile&do=view&target=eb2013-v8.2.pdf
Kumar, M. S. N., Davis, C. J., Grave, J. M. C., Ferreira, B., & Froebrich, D. 2007, MNRAS, 374, 54
Lim, W., Nakamura, F., Wu, B., et al. 2021, PASJ, 73, S239
Liow, K. Y., & Dobbs, C. L. 2020, MNRAS, 499, 1099
Liu, M., Tan, J. C., Cheng, Y., & Kong, S. 2018, ApJ, 862, 105
Luisi, M., Anderson, L. D., Schneider, N., et al. 2021, SciA, 7, eabe9511
Maia, F. F. S., Moraux, E., & Joncour, I. 2016, MNRAS, 458, 3027
Mangum, J. G., & Shirley, Y. L. 2015, PASP, 127, 266
Marston, A. P., Reach, W. T., Noriega-Crespo, A., et al. 2004, ApJS, 154, 333
Matthews, B. C., McPhee, C. A., Fissel, L. M., & Curran, R. L. 2009, ApJS, 182, 143
Motte, F., Bontemps, S., Csengeri, T., et al. 2022, A&A, 662, A8
Motte, F., Bontemps, S., & Louvet, F. 2018a, ARA&A, 56, 41
Motte, F., Bontemps, S., Schilke, P., et al. 2007, A&A, 476, 1243
Motte, F., Nony, T., Louvet, F., et al. 2018b, NatAs, 2, 478
Motte, F., Zavagno, A., Bontemps, S., et al. 2010, A&A, 518, L77
Palmeirim, P., André, P., Kirk, J., et al. 2013, A&A, 550, A38
Peretto, N., André, P., & Belloche, A. 2006, A&A, 445, 979
Peretto, N., Fuller, G. A., André, P., et al. 2014, A&A, 561, A83
Peretto, N., Fuller, G. A., Duarte-Cabral, A., et al. 2013, A&A, 555, A112
Peretto, N., Hennebelle, P., & André, P. 2007, A&A, 464, 983
Peretto, N., Lenfestey, C., Fuller, G. A., et al. 2016, A&A, 590, A72
Peters, T., Banerjee, R., Klessen, R. S., & Mac Low, M.-M. 2011, ApJ, 729, 72
Peters, T., Klessen, R. S., Mac Low, M.-M., & Banerjee, R. 2010, ApJ, 725, 134
Pound, M. W., & Wolfire, M. G. 2008, in ASP Conf. Ser. 394, Astronomical Data Analysis Software and Systems XVII, ed. R. W. Argyle, P. S. Bunclark, & J. R. Lewis (San Francisco, CA: ASP), 654
Pound, M. W., & Wolfire, M. G. 2023, AJ, 165, 25
Pouteau, Y., Motte, F., Nony, T., et al. 2022, A&A, 664, A26
Reipurth, B., & Schneider, N. 2008, in Star Formation and Young Clusters in Cygnus, ed. B. Reipurth, Vol. 4 (San Francisco, CA: ASP), 36
Risacher, C., Güsten, R., Stutzki, J., et al. 2018, JAI, 7, 1840014
Russeil, D., Zavagno, A., Motte, F., et al. 2010, A&A, 515, A55
Rygl, K. L. J., Brunthaler, A., Sanna, A., et al. 2012, A&A, 539, A79
Sanhueza, P., Contreras, Y., Wu, B., et al. 2019, ApJ, 886, 102
Schneider, N., Bonne, L., Bontemps, S., et al. 2023, NatAs, 7, 546
Schneider, N., Bontemps, S., Motte, F., et al. 2016a, A&A, 587, A74
Schneider, N., Bontemps, S., Motte, F., et al. 2016b, A&A, 591, A40
Schneider, N., Bontemps, S., Simon, R., et al. 2006, A&A, 458, 855
Schneider, N., Csengeri, T., Bontemps, S., et al. 2010, A&A, 520, A49
Schneider, N., Csengeri, T., Klessen, R. S., et al. 2015, A&A, 578, A29
Schneider, N., Ossenkopf-Okada, V., Clarke, S., et al. 2022, A&A, 666, A165
Schneider, N., Simon, R., Bontemps, S., Comerón, F., & Motte, F. 2007, A&A, 474, 873
Schneider, N., Simon, R., Guevara, C., et al. 2020, PASP, 132, 104301
Shirley, Y. L. 2015, PASP, 127, 299

Tahani, M. 2022, FrASS, 9, 940027
Tahani, M., Lupypciw, W., Glover, J., et al. 2022, A&A, 660, A97
Tahani, M., Plume, R., Brown, J. C., Soler, J. D., & Kainulainen, J. 2019, A&A, 632, A68
Tan, J. C., Beltrán, M. T., Caselli, P., et al. 2014, in Protostars and Planets VI, ed. H. Beuther et al. (Tucson, AZ: Univ. Arizona Press), 149
Teague, R. 2019, RNAAS, 3, 74
Tigé, J., Motte, F., Russeil, D., et al. 2017, A&A, 602, A77
Tiwari, M., Karim, R., Pound, M. W., et al. 2021, ApJ, 914, 117
Traficante, A., Fuller, G. A., Duarte-Cabral, A., et al. 2020, MNRAS, 491, 4310
Traficante, A., Fuller, G. A., Smith, R. J., et al. 2018a, MNRAS, 473, 4975
Traficante, A., Lee, Y. N., Hennebelle, P., et al. 2018b, A&A, 619, L7
Vaidya, B., Hartquist, T. W., & Falle, S. A. E. G. 2013, MNRAS, 433, 1258
Vallée, J. P., & Fiege, J. D. 2006, ApJ, 636, 332
van der Tak, F. F. S., Black, J. H., Schöier, F. L., Jansen, D. J., & van Dishoeck, E. F. 2007, A&A, 468, 627
Vázquez-Semadeni, E., Gómez, G. C., Jappsen, A. K., Ballesteros-Paredes, J., & Klessen, R. S. 2009, ApJ, 707, 1023
Vázquez-Semadeni, E., González-Samaniego, A., & Colín, P. 2017, MNRAS, 467, 1313
Vázquez-Semadeni, E., Palau, A., & Ballesteros-Paredes, J. 2019, MNRAS, 490, 3061
Wang, P., Li, Z.-Y., Abel, T., & Nakamura, F. 2010, ApJ, 709, 27
Watkins, E. J., Peretto, N., Marsh, K., & Fuller, G. A. 2019, A&A, 628, A21
Williams, G. M., Peretto, N., Avison, A., Duarte-Cabral, A., & Fuller, G. A. 2018, A&A, 613, A11
Wilson, T. L., & Rood, R. 1994, ARA&A, 32, 191
Wu, B., Van Loo, S., Tan, J. C., & Bruderer, S. 2015, ApJ, 811, 56
Wyrowski, F., Güsten, R., Menten, K. M., et al. 2016, A&A, 585, A149
Wyrowski, F., Güsten, R., Menten, K. M., Wiesemeyer, H., & Klein, B. 2012, A&A, 542, L15
Young, E. T., Becklin, E. E., Marcum, P. M., et al. 2012, ApJL, 749, L17
Zinnecker, H., & Yorke, H. W. 2007, ARA&A, 45, 481